machines

MDPI

Article

Research on the Influence of Radial Variation of Centroid on the Motion of Spherical Robot

Long Ma [1,2,*], Minggang Li [3], Rui Chang [1] and Hanxu Sun [3]

[1] CCTEG China Coal Research Institute, Beijing 100013, China; changrui@ccrise.cn
[2] State Key Laboratory of Intelligent Coal Mining and Strata Control, Beijing 100013, China
[3] School of Automation, Beijing University of Posts and Telecommunications, Beijing 100876, China; mgli2020@bupt.edu.cn (M.L.); hxsun@bupt.edu.cn (H.S.)
* Correspondence: malong@ccrise.cn

Abstract: Through the pendulum mechanism inside the spherical shell, the centroid can be varied circumferentially, enabling the spherical robot to achieve omnidirectional flexible movement. Additionally, the radial variation ability of the centroid enables spherical robots to adopt two distinct driving modes: the traditional lower pendulum driving mode and the inverted pendulum driving mode. There are two manifestations of radial variation in the centroid: having different radial positions of the centroid and achieving radial movement of the centroid. Focusing on these two manifestations, experimental data are obtained through different motion velocities and different motion slopes to conduct research on the influence of radial variation in the centroid on the motion of spherical robots. Based on the experimental data, multiple indicators are analyzed, including response speed, convergence speed, stability, and overshoot, as well as steering ability, climbing ability, and output power. The impact of the radial variation ability of the centroid on the control performance, locomotion capability, and energy consumption of spherical robots is summarized, and the correlation model relating the motion requirements to the radial position of the centroid is established, providing a theoretical basis for the selection of driving modes and centroid positions for spherical robots facing complex task requirements.

Keywords: spherical robot; inverted pendulum drive; radial variation of centroid; motion characteristics; pendulum length model

Citation: Ma, L.; Li, M.; Chang, R.; Sun, H. Research on the Influence of Radial Variation of Centroid on the Motion of Spherical Robot. *Machines* **2024**, *12*, 422. https://doi.org/10.3390/machines12060422

Academic Editor: Dan Zhang

Received: 7 May 2024
Revised: 1 June 2024
Accepted: 13 June 2024
Published: 19 June 2024

Copyright: © 2024 by the authors. Licensee MDPI, Basel, Switzerland. This article is an open access article distributed under the terms and conditions of the Creative Commons Attribution (CC BY) license (https://creativecommons.org/licenses/by/4.0/).

1. Introduction

Compared to conventional mobile robots, the spherical enclosed shell endows spherical robots with the capability to prevent overturning and achieve an omnidirectional fast movement while also possessing strong self-protection and low energy consumption characteristics [1,2]. These inherent advantages enable spherical robots to effectively address rapid deployment operations in hazardous and confined work environments. Since the successful development of the first spherical robot in 1996, numerous research institutions have maintained a high level of attention and continuous research on spherical robot-related technologies, with the number of related research outcomes consistently stable in internationally renowned journals such as IEEE and ASME.

Research on the driving mechanisms of spherical robots is currently focused on four main directions: wheeled eccentric torque driving mechanisms (Figure 1a), multi-wheel friction internal driving mechanisms (Figure 1b), and pendulum eccentric torque driving mechanisms (Figure 1c), as well as other novel driving mechanisms such as wind-driving mechanisms (Figure 1d), localized deformation of the spherical shell (Figure 1e), and leg-driving mechanisms (Figure 1f) [3–5]. The wheeled eccentric torque driving mechanism was the initial driving mechanism for spherical robots, achieving omnidirectional movements through the motion of a small car inside the shell, as seen in the Rollo series of

spherical robots [6]. In-depth research on this type of driving mechanism has been conducted by teams at Beijing Jiaotong University in China [7]. The multi-wheel friction internal driving mechanism enables the omnidirectional movement of spherical robots through frictional interaction between multiple friction wheels inside the shell and the inner wall of the shell. Relevant teams at National Taiwan University and Zanjan University in Iran have conducted in-depth research on this mechanism [8,9].

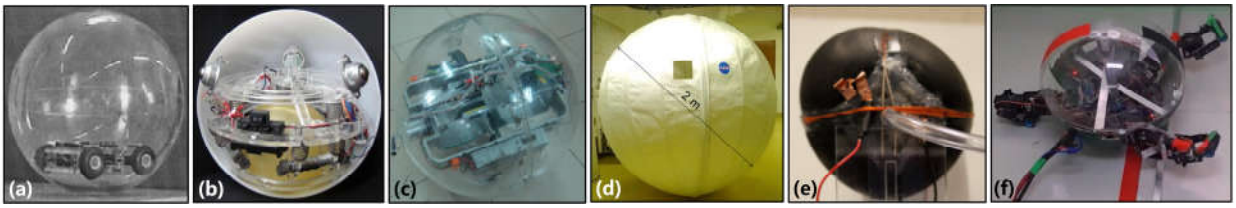

Figure 1. Different driving mechanisms of spherical robots: (**a**) a spherical robot utilizing a wheeled eccentric torque driving mechanism; (**b**) a spherical robot utilizing a multi-wheel friction internal driving mechanisms; (**c**) a spherical robot utilizing a pendulum eccentric torque driving mechanisms; (**d**) a spherical robot utilizing a wind-driving mechanisms; (**e**) a spherical robot utilizing a localized deformation of the spherical shell; (**f**) a spherical robot utilizing a leg-driving mechanisms.

With the advantages of low mechanism complexity, a simple connection between the internal mechanism and the spherical shell, and high driving efficiency, the pendulum eccentric torque (PET) is the most extensively studied driving mechanism for spherical robots [10]. As a core component within the internal mechanism of spherical robots based on the PET driving mechanism, the position of the pendulum directly affects the centroid position of the spherical robot, thereby influencing its motion state [11]. J.C. Yoon et al. designed a PET spherical robot named KisBot II, where the main shaft frame and pendulum mechanism could rotate 360° vertically inside the sphere without interfering with each other, endowing it with the ability for omnidirectional flexible movement [12]. S. Mahboubi et al. designed a spherical robot driven by dual pendulums, where two motors independently drove two symmetrically positioned pendulum mechanisms. Through the coordination between the pendulums, the spherical robot achieved linear motion, arc motion, turning in place, and hopping [13]. B.P. DeJong et al. designed a spherical robot driven by four pendulums, with the four independently movable pendulums distributed inside the spherical shell in a tetrahedral configuration. This configuration enabled the spherical robot to apply rolling torque in any direction while stationary, thereby achieving omnidirectional flexible movement [14]. M. YUE et al. proposed a horizontally collinear-driven spherical robot and a coaxial dual eccentric mass-driven ellipsoidal robot, expanding the dual-drive mechanism of the PET and enhancing motion flexibility [15]. Q. ZHAN et al. successively proposed multiple BHQ series spherical robots, among which the BHQ-2 spherical robot added a visual function to the spherical robots based on further expanding the dual-drive mechanism [16–18]. G. LI et al. designed the "Watcher" spherical robot, effectively improving the positioning and target detection capabilities of spherical robots based on multi-sensor fusion technology, promoting the effective application of pendulum eccentric torque-driven spherical robots in practical task environments [19].

The complex and ever-changing unstructured task environments are placing increasingly higher demands on the practicality of spherical robots. The improvement of practicality is aimed not only at enhancing the control performance of spherical robots but also at enhancing the diverse adaptability to different task requirements, such as long endurance and high mobility [20]. However, current research on spherical robots driven by pendulum eccentric torque has primarily concentrated on traditional variations in the swinging mechanism, specifically exploring different methods of circumferential variation, without genuinely considering the practical enhancement of spherical robots. If the pendulum possesses both circumferential and radial motion capabilities, meaning the centroid of the spherical robot can vary radially, then the pendulum can facilitate a transition

between the upper and lower hemispheres of the spherical robot. In this scenario, the spherical robot can achieve not only the traditional lower pendulum driving mode but also a new inverted pendulum driving mode (as shown in Figure 2). When the spherical robot operates in two different driving modes, the position of the pendulum can move radially. This means that the pendulum's range of motion within the spherical shell can be increased, thereby enriching the motion capabilities of the spherical robot and enhancing its ability to handle various task requirements in unstructured environments.

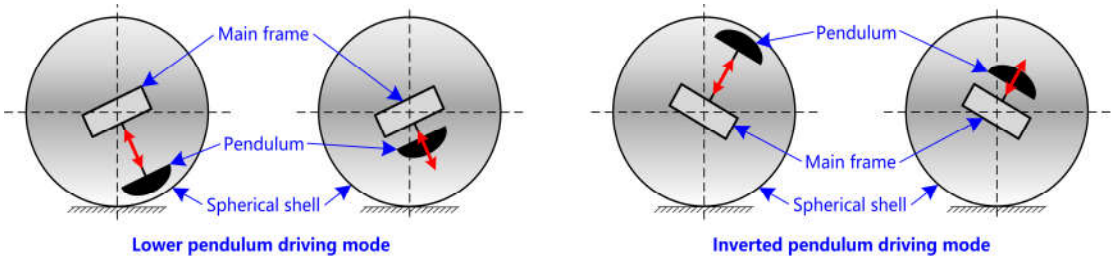

Figure 2. Two driving modes of spherical robot.

There are two manifestations of radial variation for the centroid: having different radial positions of the centroid and achieving radial movement of the centroid. For the two different driving modes of the spherical robot, we conducted experimental research using two routes: different motion velocities and different motion slopes. Following the acquisition of relevant experimental data, we analyzed the motion of the spherical robot, taking into account factors such as the control system response speed, convergence speed, stability, overshoot, steering ability, climbing ability, and output power. We then summarized the impact of the radial variation of the centroid on motion performance and theorized these findings. Additionally, we explored the mathematical model that links the motion requirements of the spherical robot to the radial position of the centroid. This research provides a foundation for selecting the driving mode and centroid position of radial-variable spherical robots for complex task requirements.

The rest of this study is organized as follows: Section 2 introduces the experimental platform and experimental settings, namely the radial variable centroid spherical robot BYQ-GS, and sets up control analysis indicators and relevant experimental parameters. Section 3 is the acquisition of motion experimental data. Section 4 analyzes the experimental data corresponding to the motion indicators and summarizes the relevant law and correlation model on the radial variable centroid spherical robot. Section 5 conducts an experimental verification of the analysis results. Section 6 summarizes the research work.

2. Experimental Platform and Experimental Settings

We used the radial variable centroid spherical robot BYQ-GS as the experimental platform and presented the spatial multi-body dynamics model for unstructured task environments. We adopted the Hierarchical Sliding Mode Control (HSMC) method to control the robot and set relevant control parameters. To obtain data corresponding to the even specified motion analysis indicators, we set the experimental parameters for the different radial positions and radial movements of the centroid.

2.1. Experimental Platform

The experimental platform adopts the radial variable centroid spherical robot BYQ-GS (Figure 3a,b), and the pendulum of the spherical robot can move radially. When the pendulum is located on the upper side or the lower side of the internal mechanism (Figure 3c,d), the centroid of the spherical robot can be located on the upper or lower hemispheres, thus achieving the lower pendulum driving mode or the inverted pendulum driving

mode. When in different driving modes, spherical robots can achieve radial variation in the centroid through the radial movement of the pendulum.

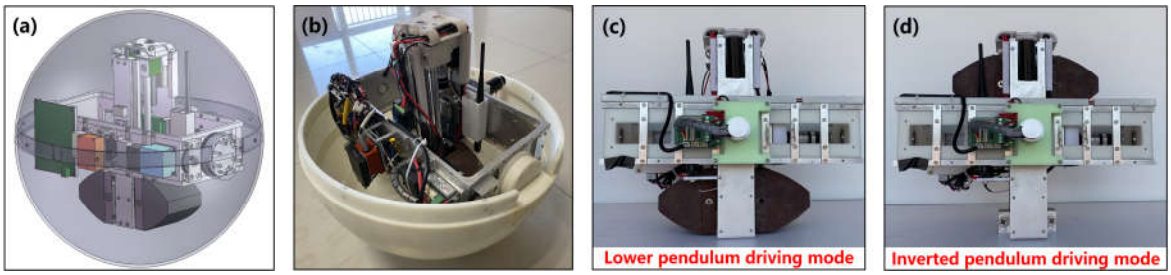

Figure 3. Prototype of spherical robot BYQ-GS: (**a**) design model; (**b**) physical model with half of the spherical shell removed; (**c**) physical model of internal structure in lower pendulum driving mode; (**d**) physical model of internal structure in inverted pendulum driving mode.

The basic performance of the spherical robot BYQ-GS is detailed in Table 1. The spherical shell is constructed from a glass fiber reinforced polymer (GFRP) composite material, with a thickness of 2.3 mm and an outer diameter of 400 mm, featuring a layup sequence of $[0/90]_6$. The control system employs a host computer to send commands, while the mobile end is responsible for receiving, processing, and executing commands. Additionally, the mobile end facilitates the transmission of real-time pose data generated by relevant sensors during motion to the host computer. The pose feedback system consists of motor encoders, an MTi-300 inertial measurement unit (IMU), and a BD992-INS multi-star multi-frequency high-precision combined navigation board (RTK). The measurement accuracy of the IMU angles is 0.05°, the theoretical positioning accuracy of RTK is 0.008 m, the velocity measurement accuracy is 0.007 m/s, and the pitch/roll angle measurement accuracy is 0.10°. This system is capable of the real-time acquisition of the global position, heading, velocity, and attitude information. After computation, we can obtain the motion state information of the spherical robot [21–23].

Table 1. Performance of spherical robot BYQ-GS.

Parameter Type	Value	Parameter Type	Value
total mass (kg)	12.8	range of pendulum length variation (m)	0.04–0.12
pendulum mass (kg)	4.7	rated velocity of pendulum radial movement (m/s)	0.03
outer radius (mm)	200	rated motion velocity (maximum pendulum length) (m/s)	4
drop height (cm)	≥25	rated acceleration (maximum pendulum length) (m/s^2)	0.7
endurance (h)	≥1	climbing capability (maximum pendulum length) (°)	10

2.2. Spatial Multi-Body Dynamics Model

When the radial variable centroid spherical robot operates in two different driving modes, its simplified model of omnidirectional multi-body motion is shown in Figure 4. Driving mode 1 is defined as the lower pendulum driving mode, and driving mode 2 is defined as the inverted pendulum driving mode.

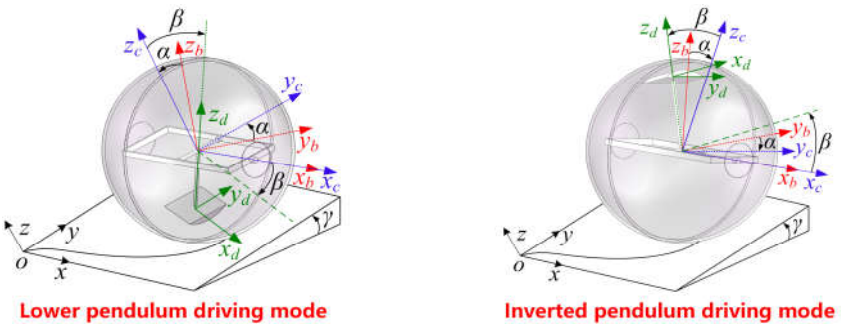

Figure 4. Simplified model for the omnidirectional multi-body motion of the radial variable centroid spherical robot.

$\boldsymbol{\Sigma}_0$ is the inertial coordinate system fixed to the slope. $\boldsymbol{\Sigma}_b$ is the coordinate system fixed to the spherical shell and rolls with it. $\boldsymbol{\Sigma}_c$ is the coordinate system fixed to the main frame and rotates with it. The coordinate origins of $\boldsymbol{\Sigma}_b$ and $\boldsymbol{\Sigma}_c$ coincide with the geometric center of the spherical shell. $\boldsymbol{\Sigma}_d$ is the coordinate system fixed to the pendulum and rotates with it, with the centroid of the pendulum as the origin. $\boldsymbol{x}_c$ and $\boldsymbol{x}_b$ constantly coincide and have the same orientation. $\boldsymbol{y}_d$ and $\boldsymbol{x}_b$ maintain the same orientation throughout. In the initial state, $\boldsymbol{\Sigma}_c$ coincides with $\boldsymbol{\Sigma}_b$, and the main frame rotates about $\boldsymbol{x}_b$ with an angle of α. Each axis of $\boldsymbol{\Sigma}_d$ remains parallel to $\boldsymbol{\Sigma}_c$, and the pendulum rotates about $\boldsymbol{y}_c$ with an angle of β. The slope angle is γ. The zyx Euler angles from $\boldsymbol{\Sigma}_0$ to $\boldsymbol{\Sigma}_b$ are denoted as (φ,θ,ψ), where φ represents the heading angle, θ represents the roll angle and ψ represents the pitch angle. The coordinates of the geometric center of the spherical shell in $\boldsymbol{\Sigma}_0$ are represented as (x,y,z), and the radius of the spherical shell is represented as R. The variable pendulum length for two different driving modes is denoted as L. The torque of the long-axis motor in the $\boldsymbol{x}_c$ direction is represented as τ_ψ, the torque of the short-axis motor in the $\boldsymbol{y}_c$ direction is represented as τ_θ, and the torque of the pendulum lifting motor in the $\boldsymbol{z}_d$ direction is represented as τ_L.

The pendulum length L of the radial variable centroid spherical robot is one of the variables. The position, attitude, and centroid position of the spherical robot can be fully described by the eight generalized coordinates in $\boldsymbol{q}$ as shown in Equation (1), while the three nonholonomic constraints can be expressed in matrix form as shown in Equation (1) [21,24,25].

$$\boldsymbol{q}=\begin{bmatrix}x & y & \varphi \vdots \theta & \psi & \alpha & \beta & L\end{bmatrix}^T \quad \boldsymbol{A}(\boldsymbol{q})\dot{\boldsymbol{q}}=0 \quad \boldsymbol{A}(\boldsymbol{q})=[\boldsymbol{A}_1 \vdots \boldsymbol{A}_2]=\begin{bmatrix} & R\cos\varphi & R\sin\varphi\cos\theta & 0 & 0 & 0 \\ \boldsymbol{I}_3 \vdots & R\sin\varphi & -R\cos\varphi\cos\theta & 0 & 0 & 0 \\ & 0 & -\sin\theta & 0 & 0 & 0 \end{bmatrix} \tag{1}$$

Based on Lagrange's equation of the first kind, the dynamic models of the radial variable centroid spherical robot for driving mode 1 and mode 2 in an ideal task environment are given by Equation (2).

$$\boldsymbol{M}_i(\boldsymbol{q})\ddot{\boldsymbol{q}}+\boldsymbol{V}_i(\boldsymbol{q},\dot{\boldsymbol{q}})=\boldsymbol{E}_i(\boldsymbol{q})\boldsymbol{\tau}+\boldsymbol{A}^T(\boldsymbol{q})\boldsymbol{\lambda} \tag{2}$$

where, $\boldsymbol{M}_i(\boldsymbol{q})\in\mathbb{R}^{8\times8}$ represents the inertia matrix, $\boldsymbol{V}_i(\boldsymbol{q},\dot{\boldsymbol{q}})\in\mathbb{R}^{8\times1}$ represents the nonlinear term, $\boldsymbol{\lambda}=[\lambda_1\ \lambda_2\ \lambda_3]^T$ represents the undetermined multiplier vector corresponding to the nonholonomic constraint, $\boldsymbol{\tau}=[\tau_\theta\ \tau_\psi\ \tau_L]^T$ represents the input torque vector, P is defined as the lead of the linear module screw, and the input transformation matrix $\boldsymbol{E}_i(\boldsymbol{q})$ can be expressed in the following form.

$$\boldsymbol{E}_i(\boldsymbol{q})=\begin{bmatrix} 0 & 0 & \sin\alpha & \cos\alpha & 0 & 0 & (-1)^i & 0 \\ 0 & 0 & 0 & 0 & 1 & -1 & 0 & 0 \\ 0 & 0 & \cos\alpha & 0 & 0 & 0 & 0 & 2\pi/m_3P \end{bmatrix} \tag{3}$$

In order to eliminate the impact of nonholonomic constraints on the dynamic model construction process, we set the output variable of the spherical robot system to $\boldsymbol{q}_3$. Under an ideal task environment, the dynamic model of the radial variable centroid spherical robot in driving mode 1 and mode 2 can be transformed into Equation (4).

$$\begin{gathered} \dot{\boldsymbol{q}}_3=\Delta\dot{\boldsymbol{q}}_2 \\ \tilde{\boldsymbol{M}}_i\Delta^{-1}\ddot{\boldsymbol{q}}_3+(\tilde{\boldsymbol{M}}_i\dot{\Delta}^{-1}+\boldsymbol{C}^T\boldsymbol{M}_i\dot{\boldsymbol{C}}\Delta^{-1})\dot{\boldsymbol{q}}_3+\boldsymbol{C}^T\boldsymbol{V}_i=\boldsymbol{C}^T\boldsymbol{E}_i\boldsymbol{\tau} \end{gathered} \tag{4}$$

where, regardless of the position of the radial variable centroid spherical robot within the state space, matrix Δ remains invertible, and

$$\tilde{\boldsymbol{M}}_i=\boldsymbol{C}^T\boldsymbol{M}_i\boldsymbol{C}\quad \boldsymbol{q}_3=\left[x,y,\alpha,\beta,L\right]^T\quad \boldsymbol{C}(\boldsymbol{q})=\begin{bmatrix}-\boldsymbol{A}_2\\ \boldsymbol{I}_{5\times5}\end{bmatrix}\quad \Delta=\begin{bmatrix}-R\cos\varphi & -R\sin\varphi\cos\theta & 0\\ -R\sin\varphi & R\cos\varphi\cos\theta & 0\\ 0 & 0 & \boldsymbol{I}_3\end{bmatrix} \tag{5}$$

According to the performance parameters of the spherical robot BYQ-GS prototype shown in Table 1, the value of τ_L is relatively small and the action time is short, so the effect on the generalized coordinate φ can be neglected. The generalized coordinates $(x,y,\varphi,\theta,\psi,\alpha,\beta,L)$ is correlated with the generalized torque (τ_ψ,τ_θ) and can be influenced by L and $\dot{L}$, but it cannot affect the variations in L and $\dot{L}$, while τ_L corresponds one-to-one with L. In order to reduce the complexity of the dynamic model, we separately set and control L and $\dot{L}$ during the control process and only set the desired value for $(x,y,\varphi,\theta,\psi,\alpha,\beta,L)$ in the control strategy. The dynamic model for unstructured task environments, based on the ideal task environment shown in Equation (4), is represented by Equation (6).

$$\boldsymbol{M}(\boldsymbol{q})\ddot{\boldsymbol{q}}+\boldsymbol{N}(\boldsymbol{q},\dot{\boldsymbol{q}})=\boldsymbol{\tau}_m=\boldsymbol{\tau}+\boldsymbol{\tau}_{fx}+\boldsymbol{\tau}_{fn}+\boldsymbol{\tau}_{dv}+\boldsymbol{\tau}_{du}=\boldsymbol{\tau}+\boldsymbol{\tau}_{fc}+\boldsymbol{\tau}_{\xi} \tag{6}$$

where, $\boldsymbol{\tau}_m$ represents the output torque of the motor, $\boldsymbol{\tau}_f$ represents the friction term of motion, and $\boldsymbol{\tau}_d$ represents the disturbance from the mechanism or external environment. According to whether the disturbance is controllable, $\boldsymbol{\tau}_d$ is divided into controllable part $\boldsymbol{\tau}_{dv}$ and uncontrollable part $\boldsymbol{\tau}_{du}$, and $\boldsymbol{\tau}_f$ is divided into linear part $\boldsymbol{\tau}_{fx}$ and nonlinear part $\boldsymbol{\tau}_{fn}$. The controllable compensating torque $\boldsymbol{\tau}_{fc}$ is used to represent $\boldsymbol{\tau}_{dv}$ and $\boldsymbol{\tau}_{fx}$, which mainly comes from the rolling friction couple moment exerted by the ground on the spherical shell, as well as the friction torque inside the joint caused by the viscous damping of the bearing. The uncertain factor $\boldsymbol{\tau}_{\xi}$ is used to represent $\boldsymbol{\tau}_{du}$ and $\boldsymbol{\tau}_{fn}$.

According to Equation (6), in unstructured environments, the motion control of a spherical robot needs to consider three aspects: parameters related to the robot itself, controllable factors during motion, and uncertain and uncontrollable factors during motion. $\boldsymbol{\xi}(t,\boldsymbol{u}(t))$ is used to represent uncertain terms, which include uncertain factors such as uncontrollable bounded unknown disturbances and nonlinear friction. We convert Equation (6) into the form shown in Equation (7) and further express it as the state space expression of the subsystem shown in Equation (8) and the generalized coordinate $i\in(x,y,\alpha,\beta)$ [16].

$$\ddot{\boldsymbol{q}}=f(\boldsymbol{q},\dot{\boldsymbol{q}},t)+g(\boldsymbol{q},t)\boldsymbol{u}(t)+\boldsymbol{\xi}(t,\boldsymbol{u}(t)) \tag{7}$$

$$\ddot{q}_i=f_i+g_iu_i+\xi_i \tag{8}$$

where, $f(\boldsymbol{q},\dot{\boldsymbol{q}},t)=(f_1 \ldots f_i)^T=-\boldsymbol{M}(\boldsymbol{q})^{-1}\boldsymbol{N}(\boldsymbol{q},\dot{\boldsymbol{q}})$ $\boldsymbol{g}(\boldsymbol{q},t)=(g_1 \ldots g_i)^T=\boldsymbol{M}(\boldsymbol{q})^{-1}$ $\boldsymbol{u}(t)=(u_1 \ldots u_i)^T=\boldsymbol{\tau}+\boldsymbol{\tau}_{fc}$ $\boldsymbol{\xi}(t,u(t))=(\xi_1 \ldots \xi_i)^T$.

2.3. Experimental Settings

The radial variation of a spherical robot's centroid manifests in two forms: having different radial positions of the centroid during motion and achieving radial movement of the centroid during motion. When conducting motion research on spherical robots exhibiting these two manifestations, it is necessary to consider the evaluation indicators for motion and methods for obtaining experimental data.

2.3.1. Evaluation Indicators for Motion

The setting of control evaluation indicators and the method for obtaining experimental data are shown in Figure 5. We divided the motion evaluation indicators of spherical robots into three aspects: control performance, locomotion capability, and energy consumption. Control performance was comprehensively analyzed through four indicators of the control system: response speed, convergence speed, stability, and overshoot. Locomotion capability is analyzed through two indicators: steering ability and climbing ability. We obtained experimental data for these indicators through two routes. The first route is motion with different expected velocities on the horizontal plane, and the experimental scene is an outdoor track and field runway. We conducted experiments by combining different pendulum lengths L with different expected velocities v_d. The second route is motion with different slope angles, and the experimental venue is a wooden slope measuring 2.5 m × 2.5 m. The slope angle can be adjusted by varying the number and position of wooden blocks underneath the slope. We conducted experiments by combining different pendulum lengths L and slope angles γ.

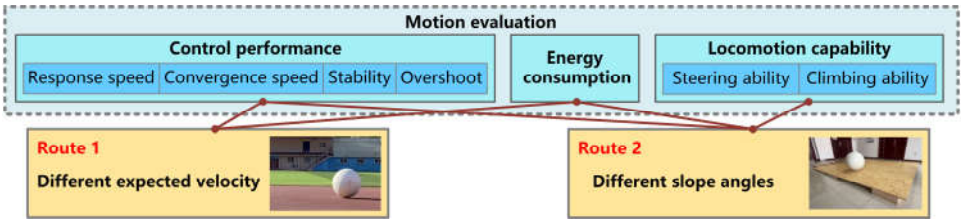

Figure 5. The setting of control evaluation indicators and the method for obtaining data.

The data for motion evaluation indicators are based on the motion position error of the spherical shell $e_x(t)=p_x(t)-x(t)$ and the swing position error of the pendulum $e_\alpha(t)=p_\alpha(t)-\alpha(t)$. Here, $p_x(t)$ and $p_\alpha(t)$ represent the theoretical values of the real-time position, while $x(t)$ and $\alpha(t)$ represent the actual values of the real-time position. The experimental data corresponding to each indicator are as follows.

2.3.2. Parameter Settings for Controller

We defined the first layer of the sliding surface $S_i(t)$, the second layer of the sliding surface $S(t)$, and the exponential approach law $\dot{S}$ of the spherical shell subsystem, main frame subsystem, and pendulum subsystem, respectively, as presented below.

$$S_i(t)=\dot{e}_i(t)+a_i e_i(t) \qquad S(t)=\sum c_i S_i(t) \qquad \dot{S}=-\varepsilon_1 \tanh(S)-\varepsilon_2 S \tag{9}$$

where, $e_i(t)$ represents the difference between the expected value $p_i(t)$ and the real-time value $i(t)$ of the generalized coordinates, $i\in(x,y,\alpha,\beta)$. The controller parameter settings for different routes are shown in Table 2 [26–28].

Table 2. The controller parameter settings for different routes.

Route	$(a_x, a_y, a_\alpha, a_\beta)$	$(c_x, c_y, c_\alpha, c_\beta)$	$(\varepsilon_1, \varepsilon_2)$
1	(0.83, 7.26, 2.85, 0.21)	(8.81, 1.73, 2.18, 0.94)	(5.45, 1.97)
2	(1.47, 11.82, 0.78, 4.19)	(15.62, 0.94, 5.65, 7.17)	(2.56, 5.44)

2.3.3. Parameter Settings for Experiment

Experiment type 1 involved different radial positions of the centroid, with the pendulum length L remaining constant during motion. Experiment type 2 involved radial movement of the centroid, where the pendulum length transitioned from the initial length L_0 to the target length L_d at a constant speed of 0.01 m/s at the beginning of motion. Based on Equation (10), we analyzed the impact of the radial movement of the centroid on the motion evaluation indicators during the motion process. Each type of experiment was conducted through two different routes, and we compared the motion evaluation indicators of spherical robots in two different driving modes. The selected parameters for the experiments, including expected velocities v_d and slope angles γ, as well as the initial and desired states of the control system, are all shown in Figure 6.

$$\kappa_i = indicator\ data_{i(L_0 \to L_d)} \,/\, indicator\ data_{i(L_0)} \tag{10}$$

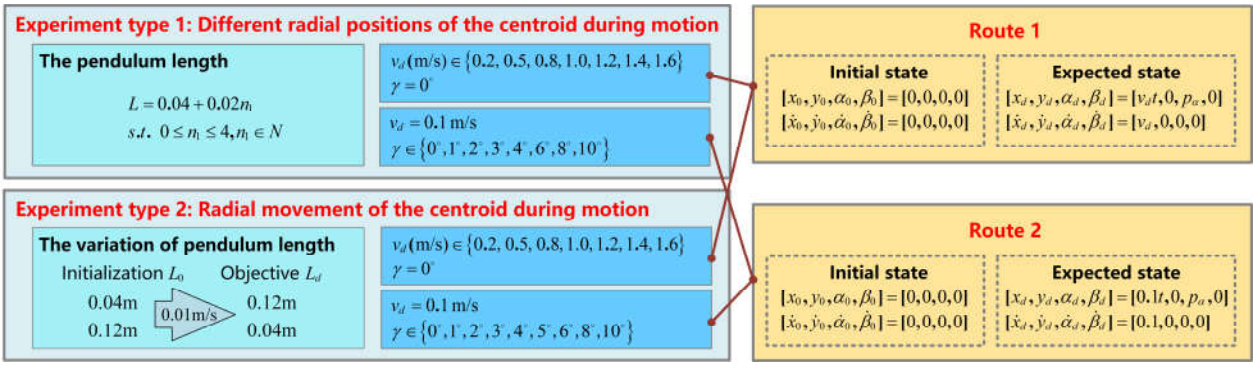

Figure 6. Parameter settings for experiment.

Due to the influence of the rolling resistance couple moment on the motion process, for the swing angle α and β, as shown in Figure 4, the theoretical equilibrium angles are p_α and p_β in the state of motion convergence and can be determined by considering the relevant descriptions in References [29,30]. With the premise that the system can converge, we analyzed the experimental results of the lower pendulum driving mode and inverted pendulum driving mode based on the evaluation indicators for motion. To ensure the reliability of the experimental data and facilitate a more intuitive comparison of the results, we repeated the experiment five times and calculated the average of the obtained data. We then preprocessed the experimental data using the Savitzky–Golay smoothing algorithm (window size: 40, polynomial degree: 2) to obtain the final dataset for the experiment [31,32].

We normalized the mathematical models constructed for different indicators using Equation (11), which maps the data to the (0, 1) range for processing. This approach ensures the data retain their original distribution while also making the variation patterns of the relevant indicators more universal and eliminating the dimensional effects of different indicators during the construction process of the correlation model [33].

$$\mathrm{Norm}(z) = (z - z_{\min}) / (z_{\max} - z_{\min}) \tag{11}$$

We used the least squares method to fit the n data obtained from the experiment. According to the error theory analysis method, the fitting accuracy of the fitting value

$f(x_i, y_i)$ relative to the actual value z_i of the coordinate points is represented by Equation (12) [34,35].

$$\sigma_f = \sqrt{\sum_{i=1}^{n} \left(f(x_i, y_i) - z_i \right)^2 \Big/ (n-3)} \tag{12}$$

3. Acquisition of Motion Experimental Data

The motion evaluation of spherical robots was divided into three aspects: control performance, locomotion capability, and energy consumption. Therefore, we collected and processed experimental data of multiple evaluation indicators in the above three aspects, respectively.

Experiment type one involved experiments with different radial positions of the centroid during motion. The blue symbols represent the experimental data of the lower pendulum driving mode, while the red symbols represent the experimental data of the inverted pendulum driving mode. We applied the least squares method to formally fit the experimental data, with undetermined coefficients rounded to two decimal places. Subsequently, we established its mathematical model and calculated the fitting accuracy of the mathematical model according to Equation (12). In the mathematical model, i represents two different driving modes, and j represents two different routes for obtaining experimental data. To eliminate the influence of indicator dimensions and provide a visual analysis of the motion of the spherical robot BYQ-GS under different pendulum lengths, we normalized the fitted equations based on Equation (11). Here, $i=1$ refers to the lower pendulum driving mode, and $i=2$ refers to the inverted pendulum driving mode. By inputting the actual values of the pendulum length L, expected velocity v_d, and slope angle γ into the fitted equations, the indicator value under two different driving modes can be obtained. The range of pendulum length L is [0.04, 0.12]. The range of v_d is [0.2, 1.6]. The range of γ corresponding to L is less than the maximum slope angle defined in Figure 6. The variation range of the indicator value is [0, 1], where smaller values indicate better indicator performance.

Experiment type two involved experiments with a radial movement of the centroid during motion. The radial movement of the centroid was achieved through pendulum radial movement, which can be divided into two directions, as shown in Figure 6: pendulum length gradually increased from 0.04 m to 0.12 m, and pendulum length gradually decreased from 0.12 m to 0.04 m. The blue symbols represent experimental data. We analyzed the experimental data and summarized the change trend according to Equation (10).

3.1. Control Performance

As shown in Figure 6, the evaluation indicators for control performance were divided into four aspects: response speed, convergence speed, stability, and overshoot.

3.1.1. Response Speed

We evaluated the response speed of the control system of the spherical robot BYQ-GS under two different driving modes by means of Route 1 and Route 2. The evaluation indicators were the generation time of maximum torque $t_{\tau-\max}$.

Experiment type 1: The trends of $t_{\tau-\max}$ are shown in Figure 7. When the pendulum length, target parameters, and environmental parameters of the spherical robot were consistent under two different driving modes, $0.12\text{s} \le t_{\tau-\max 1} - t_{\tau-\max 2} \le 0.32\text{s}$ (Tables S1–S4). The experimental data shown in Figure 7 were fitted with a mathematical model, and the fitting results can be represented by Equation (13).

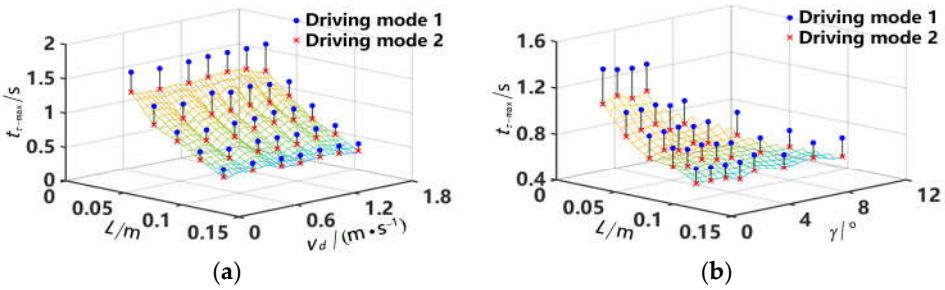

Figure 7. Experimental data of $t_{\tau-\max}$ obtained from experiments with different radial positions of the centroid. (**a**) Route 1, (**b**) Route 2.

$$t_{\tau-\max} = K^{(i)}_{\text{Route}-j} = a_1x^3 + a_2y^3 + a_3x^2 + a_4y^2 + a_5x + a_6y + a_7x^2y + a_8xy^2 + a_9xy + a_{10} \quad (13)$$

The coefficients of Equation (13) are presented in Table 3. According to Equation (12), the maximum fitting accuracy of $t_{\tau-\max 1}$ and $t_{\tau-\max 2}$ to the experimental data is 0.155 s, which does not affect our ability to assess the trend of the experimental data.

Table 3. The coefficients for Equation (13).

		x, *y*	a_1	a_2	a_3	a_4	a_5	a_6	a_7	a_8	a_9	a_{10}
$t_{\tau-\max 1}$	$K^{(1)}_{\text{Route\_1}}$	L, v_d	−884.82	−0.14	321.30	0.38	−46.99	−0.28	−1.52	0.10	−0.16	3.14
	$K^{(1)}_{\text{Route\_2}}$	L, γ	−1215.67	0.01	385.97	−0.01	−45.27	−0.03	6.28	−0.02	1.11	2.72
$t_{\tau-\max 2}$	$K^{(2)}_{\text{Route\_1}}$	L, v_d	−1358.33	−0.18	416.85	0.46	−50.16	−0.39	−4.53	0.63	−0.17	2.88
	$K^{(2)}_{\text{Route\_2}}$	L, γ	−1149.95	0.01	341.22	−0.01	−37.57	0.01	−0.58	−0.03	0.12	2.19

Based on Equation (11), the response speed of the control system $K^{(i)}_{\text{Norm}}(L, v_d, \gamma)$ under driving mode one and driving mode two can be represented by Equation (14).

$$K^{(i)}_{\text{Norm}}(L, v_d, \gamma) = \text{Norm}\left[\sum_{s=1}^{2} \text{Norm}\left(K^{(i)}_{\text{Route\_}s}\right) \Big/ 2\right] \quad (14)$$

Experiment type 2: The trends of $t_{\tau-\max 1}$ and $t_{\tau-\max 2}$ are shown in Figure 8. According to the Equation (10), $\kappa_i = t_{\tau-\max i\,(L_0 \to L_d)} / t_{\tau-\max i\,(L_0)}$ (Tables S6–S9).

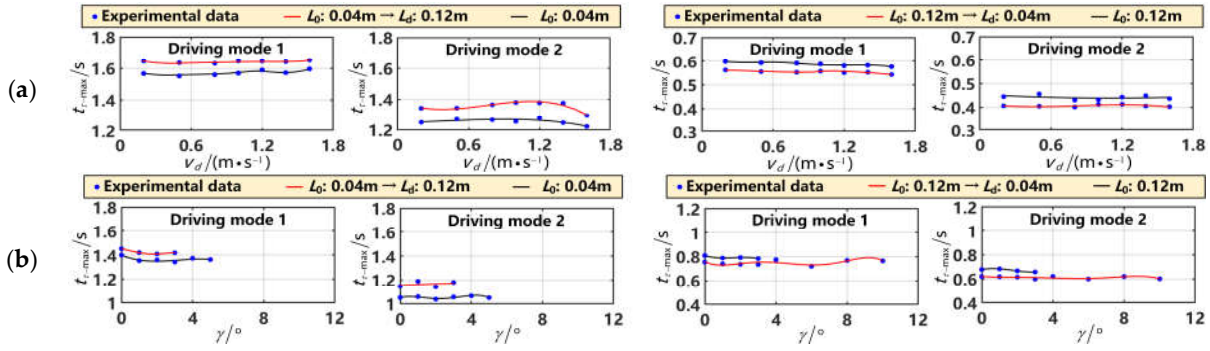

Figure 8. Experimental data of $t_{\tau-\max}$ obtained from experiments with radial movement of the centroid. (**a**) Route 1, (**b**) Route 2.

We analyzed the experimental data of the response speed of the control system, and the results of the analysis are presented in Table 4.

Table 4. The results of the analysis for the experimental data of the response speed $t_{\tau-\max}$.

		The Pendulum Length Transitioned from L_0 to L_d	
		L_0 : **0.04m** L_d : **0.12m**	L_0 : **0.12m** L_d : **0.04m**
Route 1	κ_1	[89.67%, 94.13%]	[108.99%, 112.06%]
v_d (m/s): 0.2 → 1.6	κ_2	[84.71%, 91.20%]	[113.93%, 116.12%]
Route 2	κ_1	[93.64%, 96.51%]	[105.51%, 108.55%]
γ : 0° → 10°	κ_2	[86.05%, 91.79%]	[109.34%, 113.58%]

3.1.2. Convergence Speed

We evaluated the convergence speed of the control system of the spherical robot BYQ-GS under two different driving modes by means of Route 1 and Route 2. The evaluation indicators were the motion convergence time t_r, and the motion convergence state can be determined using Equation (15).

$$-0.1|e_{\max}-e_{\min}| \le e \le 0.1|e_{\max}-e_{\min}| \tag{15}$$

Experiment type 1: The trends of t_r are shown in Figure 9. The pendulum length, target parameters, and environmental parameters of the spherical robot were consistent under two different driving modes, $0.48\text{s} \le t_{r2}-t_{r1} \le 6.30\text{s}$ (Tables S1–S4). The experimental data shown in Figure 9 were fitted with a mathematical model, and the fitting results can be represented by Equation (16).

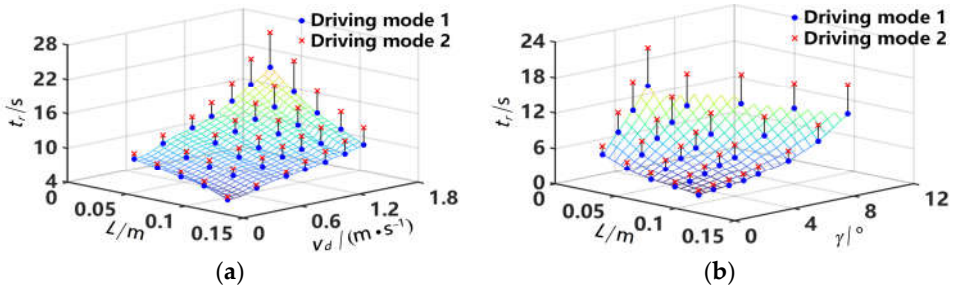

Figure 9. Experimental data of t_r obtained from experiments with different radial positions of the centroid. (**a**) Route 1, (**b**) Route 2.

$$t_{ri} = F^{(i)}_{\text{Route}-j} = a_1x^3 + a_2y^3 + a_3x^2 + a_4y^2 + a_5x + a_6y + a_7x^2y + a_8xy^2 + a_9xy + a_{10} \tag{16}$$

The coefficients of Equation (16) are presented in Table 5. According to Equation (12), the maximum fitting accuracy of t_{r1} and t_{r2} to the experimental data is 0.171 s, which does not affect our ability to assess the trend of the experimental data.

Table 5. The coefficients for Equation (16).

		x, y	a_1	a_2	a_3	a_4	a_5	a_6	a_7	a_8	a_9	a_{10}
t_{r1}	$F^{(1)}_{\text{Route\_1}}$	L, v_d	−10,252.34	−1.98	3414.05	15.92	−400.65	−8.09	−324.44	−96.94	108.19	24.64
	$F^{(1)}_{\text{Route\_2}}$	L, γ	−15,154.5	0.01	4332.2	0.16	−436.34	7.06	356.04	−1.29	−99.2	20.08
t_{r2}	$F^{(2)}_{\text{Route\_1}}$	L, v_d	−8911.1	1.05	3283.28	16.58	−434.59	8.56	−307.23	−160.61	163.14	28.88
	$F^{(2)}_{\text{Route\_2}}$	L, γ	−14,975.63	0.01	4393.38	0.16	−457.49	8.31	418.84	−1.32	−116.84	21.58

Based on Equation (11), the convergence speed of the control system $F^{(i)}_{\text{Norm}}(L, v_d, \gamma)$ under driving mode one and mode two can be represented by Equation (17).

$$F^{(i)}_{\text{Norm}}(L, v_d, \gamma) = \text{Norm}\left[\sum_{s=1}^{2}\text{Norm}\left(F^{(i)}_{\text{Route\_}s}\right)\Big/2\right] \tag{17}$$

Experiment type 2: The trends of t_{r1} and t_{r2} are shown in Figure 10. According to the Equation (10), $\kappa_i = t_{ri(L_0 \to L_d)} / t_{ri(L_0)}$ (Tables S6–S9).

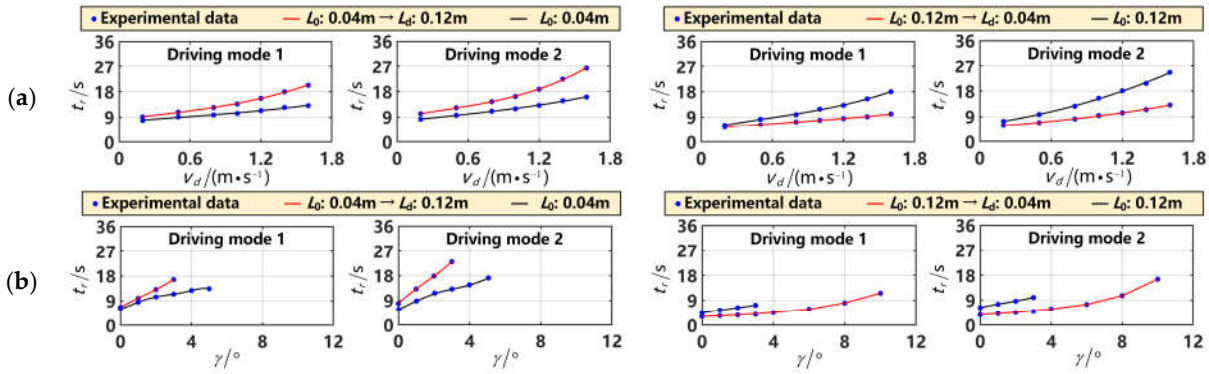

Figure 10. Experimental data of t_r obtained from experiments with radial movement of the centroid. (**a**) Route 1, (**b**) Route 2.

We analyzed the experimental data of the convergence speed of the control system, and the results of the analysis are presented in Table 6.

Table 6. The results of the analysis for the experimental data of the convergence speed t_r.

		The Pendulum Length Transitioned from L_0 to L_d	
		L_0 : 0.04m L_d : 0.12m	L_0 : 0.12m L_d : 0.04m
Route 1	κ_1	85.99% → 64.30%	113.63% → 178.52%
v_d (m/s): 0.2 → 1.6	κ_2	80.67% → 61.02%	126.64% → 188.33%
Route 2	κ_1	92.54% → 68.33%	142.06% → 186.14%
γ : 0° → 10°	κ_2	87.55% → 50.64%	169.32% → 203.98%

3.1.3. Stability

We evaluated the stability of the control system of the spherical robot BYQ-GS under two different driving modes by means of Route 1 and Route 2. The evaluation indicators were the root mean square error of position error e_{rmse} when motion is unconverged, including the position of the spherical shell $e_{x\text{–rmse}}$ and the position of the pendulum $e_{\alpha\text{–rmse}}$.

Experiment type 1: The trends of $e_{x\text{–rmse}}$ and $e_{\alpha\text{–rmse}}$ are shown in Figure 11. The pendulum length, target parameters, and environmental parameters of the spherical robot were consistent under two different driving modes, $0.109\text{m} \le e_{x\text{–rmse2}} - e_{x\text{–rmse1}} \le 1.721\text{m}$, $0.026\text{rad} \le e_{\alpha\text{–rmse2}} - e_{\alpha\text{–rmse1}} \le 0.154\text{rad}$ (Tables S1–S4). The experimental data shown in Figure 11 were fitted with a mathematical model, and the fitting results can be represented by Equation (18).

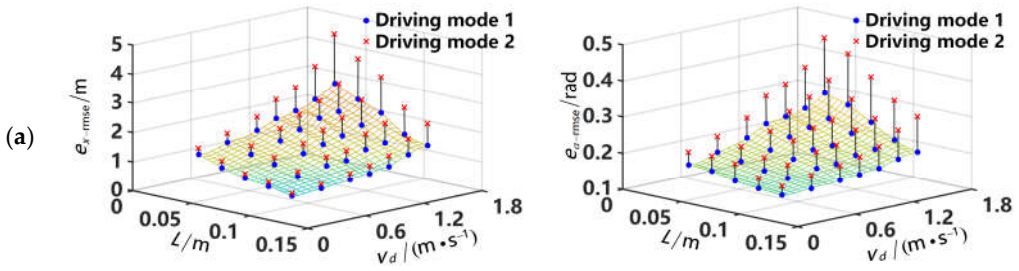

(**b**)

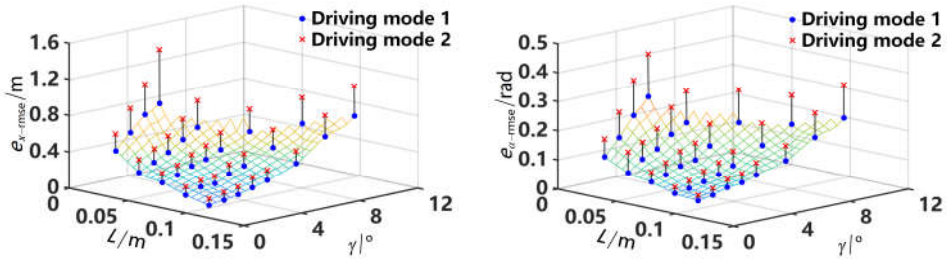

Figure 11. Experimental data of $e_{x-\mathrm{rmse}}$ and $e_{\alpha-\mathrm{rmse}}$ obtained from experiments with different radial positions of the centroid. (**a**) Route 1, (**b**) Route 2.

$$e_{\mathrm{rmse}i} = H^{(i)}_{\mathrm{Route}-j} = a_1x^3 + a_2y^3 + a_3x^2 + a_4y^2 + a_5x + a_6y + a_7x^2y + a_8xy^2 + a_9xy + a_{10} \quad (18)$$

The coefficients of Equation (18) are presented in Table 7. According to Equation (12), the maximum fitting accuracy of $e_{x-\mathrm{rmse1}}$, $e_{x-\mathrm{rmse2}}$, $e_{\alpha-\mathrm{rmse1}}$ and $e_{\alpha-\mathrm{rmse2}}$ to the experimental data are 0.0236 m, 0.0203 m, 0.0091 rad, and 0.0074 rad, respectively, which does not affect our ability to assess the trend of the experimental data.

Table 7. The coefficients for Equation (18).

		x, y	a_1	a_2	a_3	a_4	a_5	a_6	a_7	a_8	a_9	a_{10}
$e_{x\text{-rmse1}}$	$H^{(1)}_{x-\mathrm{Route\_1}}$	L, v_d	850.90	0.10	−197.58	−0.12	9.15	0.67	−21.13	0.39	−1.67	0.71
	$H^{(1)}_{x-\mathrm{Route\_2}}$	L, γ	−908.33	−0.01	237.48	0.01	−21.20	0.14	10.45	0.01	−2.35	0.75
$e_{\alpha\text{-rmse1}}$	$H^{(1)}_{\alpha-\mathrm{Route\_1}}$	L, v_d	61.46	−0.01	−16.44	0.02	1.23	0.04	1.63	−0.01	−0.58	0.06
	$H^{(1)}_{\alpha-\mathrm{Route\_2}}$	L, γ	−54.94	−0.01	16.03	0.01	−1.67	0.02	1.91	−0.01	−0.42	0.08
$e_{x\text{-rmse2}}$	$H^{(2)}_{x-\mathrm{Route\_1}}$	L, v_d	1101.19	0.38	−269.16	−0.20	13.83	0.89	−13.53	−3.24	−0.64	0.74
	$H^{(2)}_{x-\mathrm{Route\_2}}$	L, γ	−1278.90	−0.01	334.51	0.01	−29.85	0.20	15.99	0.01	−3.54	1.05
$e_{\alpha\text{-rmse2}}$	$H^{(2)}_{\alpha-\mathrm{Route\_1}}$	L, v_d	85.71	0.01	−22.75	0.01	1.68	0.05	2.24	−0.19	−0.59	0.07
	$H^{(2)}_{\alpha-\mathrm{Route\_2}}$	L, γ	−72.83	0.01	21.28	0.01	−2.22	0.03	2.56	−0.01	−0.56	0.10

Based on Equation (11), we normalized the eight fitted equations represented by Equation (18); that is, the stability of the control system $H^{(i)}_{\mathrm{Norm}}(L, v_d, \gamma)$ under driving modes one and two can be represented by Equation (19).

$$H^{(i)}_{\mathrm{Norm}}(L, v_d, \gamma) = \mathrm{Norm}\left\{\sum_{s=1}^{2}\left[\mathrm{Norm}\left(H^{(i)}_{x-\mathrm{Route\_}s}\right) + \mathrm{Norm}\left(H^{(i)}_{\alpha-\mathrm{Route\_}s}\right)\right] \Big/ 4\right\} \quad (19)$$

Experiment type 2: The trends of $e_{x-\mathrm{rmse}}$ and $e_{\alpha-\mathrm{rmse}}$ are shown in Figure 12. According to the Equation (10), $\kappa_i = \left[\left(e_{x-\mathrm{rmse}(L_0 \to L_d)} / e_{x-\mathrm{rmse}(L_0)}\right) + \left(e_{\alpha-\mathrm{rmse}(L_0 \to L_d)} / e_{\alpha-\mathrm{rmse}(L_0)}\right)\right] / 2$ (Tables S6–S9).

(**a**)

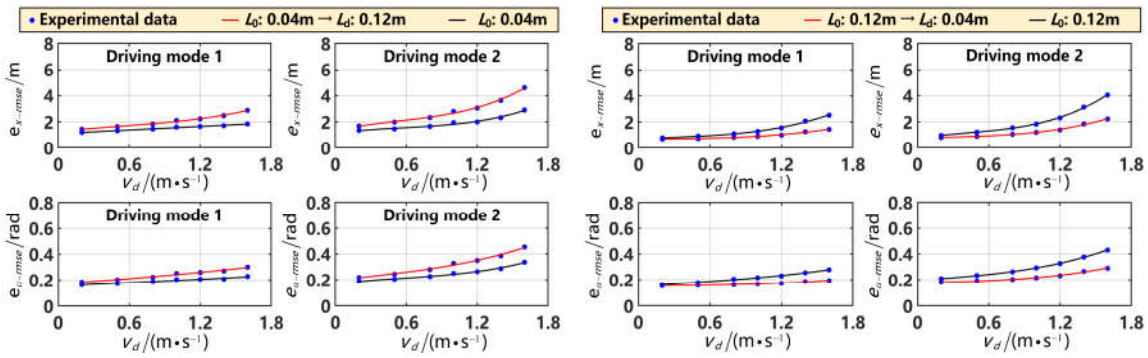

(**b**)

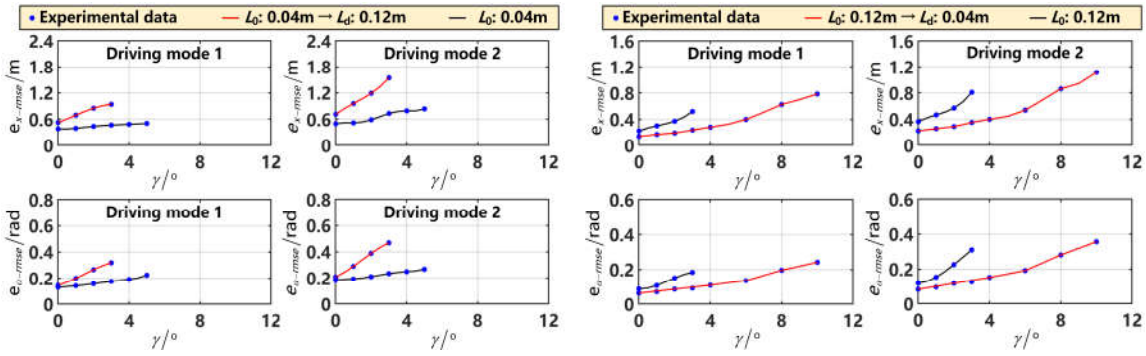

Figure 12. Experimental data of $e_{x\text{–rmse}}$ and $e_{\alpha\text{–rmse}}$ obtained from experiments with radial movement of the centroid. (**a**) Route 1, (**b**) Route 2.

We analyzed the experimental data on the stability of the control system, and the results of the analysis are presented in Table 8.

Table 8. The results of the analysis for the experimental data of the stability e_{rmse}.

		The Pendulum Length Transitioned from L_0 to L_d	
		L_0 : 0.04m L_d : 0.12m	L_0 : 0.12m L_d : 0.04m
Route 1	κ_1	85.84% → 67.09%	108.30% → 120.91%
v_d (m/s): 0.2 → 1.6	κ_2	76.38% → 61.72%	159.41% → 170.24%
Route 2	κ_1	81.27% → 52.45%	141.02% → 172.72%
γ : 0° → 10°	κ_2	78.85% → 48.80%	152.07% → 189.78%

3.1.4. Overshoot

We evaluated the overshoot of the control system of the spherical robot BYQ-GS under two different driving modes by means of Route 1 and Route 2. The evaluation indicators were the maximum absolute value of motion position error $|e|_{\max}$, including the position of the spherical shell $|e_x|_{\max}$ and the position of the pendulum $|e_\alpha|_{\max}$.

Experiment type 1: The trends of $|e_x|_{\max}$ and $|e_\alpha|_{\max}$ are shown in Figure 13. The pendulum length, target parameters, and environmental parameters of the spherical robot were consistent under two different driving modes, $0.023\text{m} \le |e_x|_{\max 1} - |e_x|_{\max 2} \le 0.249\text{m}$ and $0.022\text{rad} \le |e_\alpha|_{\max 1} - |e_\alpha|_{\max 2} \le 0.235\text{rad}$ (Tables S1–S4). The experimental data shown in Figure13 were fitted with a mathematical model, and the fitting results can be represented by Equation (20).

(**a**)

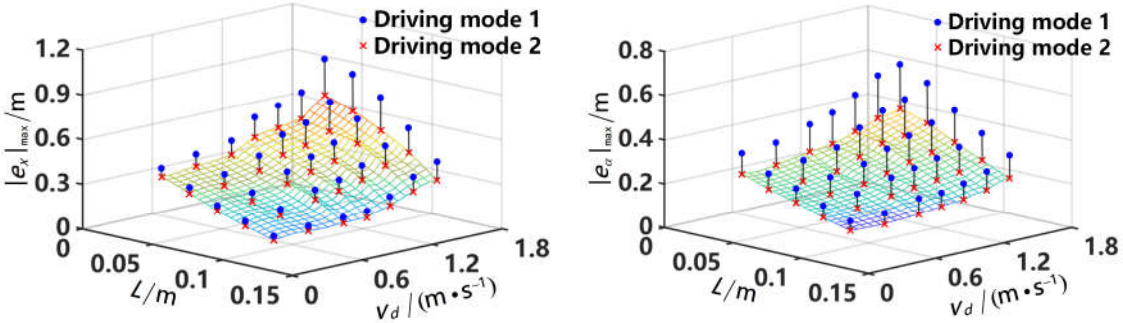

(**b**)

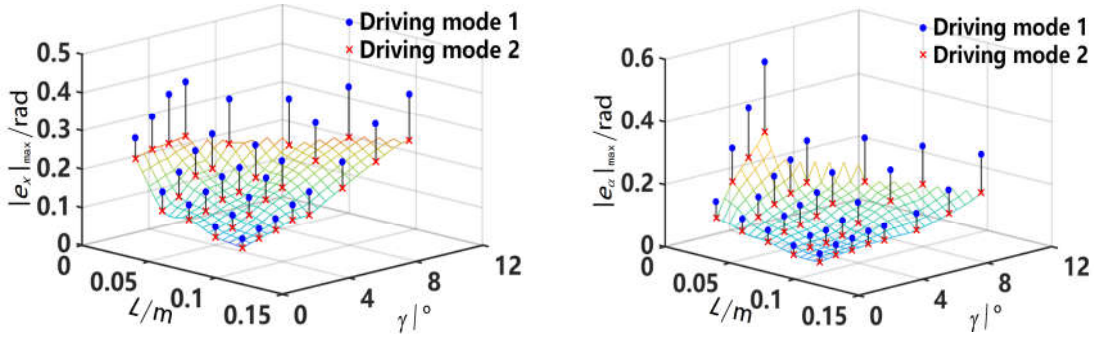

Figure 13. Experimental data of $|e_x|_{\max}$ and $|e_\alpha|_{\max}$ obtained from experiments with different radial positions of the centroid. (**a**) Route 1, (**b**) Route 2.

$$|e|_{\max i} = G^{(i)}_{\text{Route}-j} = a_1x^3 + a_2y^3 + a_3x^2 + a_4y^2 + a_5x + a_6y + a_7x^2y + a_8xy^2 + a_9xy + a_{10} \quad (20)$$

The coefficients of Equation (20) are presented in Table 9. According to Equation (12), the maximum fitting accuracy of $|e_x|_{\max 1}$, $|e_x|_{\max 2}$, $|e_\alpha|_{\max 1}$ and $|e_\alpha|_{\max 2}$ to the experimental data are 0.0124 m, 0.0101 m, 0.0137 rad and 0.0117 rad, respectively, which does not affect our ability to assess the trend of the experimental data.

Table 9. The coefficients for Equation (20).

		x, y	a_1	a_2	a_3	a_4	a_5	a_6	a_7	a_8	a_9	a_{10}
$\|e_x\|_{\max 1}$	$G^{(1)}_{x-\text{Route}\_1}$	L, v_d	−112.79	0.07	45.6	0.04	−8.46	−0.1	−50.63	−0.4	6.99	0.71
	$G^{(1)}_{x-\text{Route}\_2}$	L, γ	−658.78	−0.01	117.29	0.01	−16.36	0.05	−2.38	−0.01	−0.61	0.62
$\|e_\alpha\|_{\max 1}$	$G^{(1)}_{\alpha-\text{Route}\_1}$	L, v_d	−70.53	−0.04	22.08	0.02	−4.34	−0.06	−9.3	−0.35	0.87	0.5
	$G^{(1)}_{\alpha-\text{Route}\_2}$	L, γ	−1320.96	0.01	344.28	0.01	−29.24	0.23	17.99	−0.05	−4.02	0.93
$\|e_x\|_{\max 2}$	$G^{(2)}_{x-\text{Route}\_1}$	L, v_d	−88.84	0.04	34.55	0.09	−7.04	−0.19	−41.64	−0.56	6.34	0.65
	$G^{(2)}_{x-\text{Route}\_2}$	L, γ	−425.77	−0.01	114.28	0.01	−10.57	0.03	−1.17	−0.02	−0.32	0.43
$\|e_\alpha\|_{\max 2}$	$G^{(2)}_{\alpha-\text{Route}\_1}$	L, v_d	−61.45	0.03	19.5	0.18	−3.95	−0.12	−9.02	−0.35	1.26	0.47
	$G^{(2)}_{\alpha-\text{Route}\_2}$	L, γ	−795.22	0.01	212.73	0.01	−18.58	0.13	8.46	−0.02	−2.03	0.61

Based on Equation (11), we normalized the eight fitted equations represented by Equation (20); that is, the overshoot of the control system $G^{(i)}_{\text{Norm}}(L, v_d, \gamma)$ under driving modes one and two can be represented by Equation (21).

$$G^{(i)}_{\text{Norm}}(L, v_d, \gamma) = \text{Norm}\left\{\sum_{s=1}^{2}\left[\text{Norm}\left(G^{(i)}_{x-\text{Route}\_s}\right) + \text{Norm}\left(G^{(i)}_{\alpha-\text{Route}\_s}\right)\right] \Big/ 4\right\} \quad (21)$$

Experiment type 2: The trends of $|e_x|_{\max}$ and $|e_\alpha|_{\max}$ are shown in Figure 14. According to the analysis method represented by Equation (10), $\kappa_i = \left[\left(|e_x|_{\max(L_0 \to L_d)} / |e_x|_{\max(L_0)}\right) + \left(|e_\alpha|_{\max(L_0 \to L_d)} / |e_\alpha|_{\max(L_0)}\right)\right] / 2$ (Tables S6–S9).

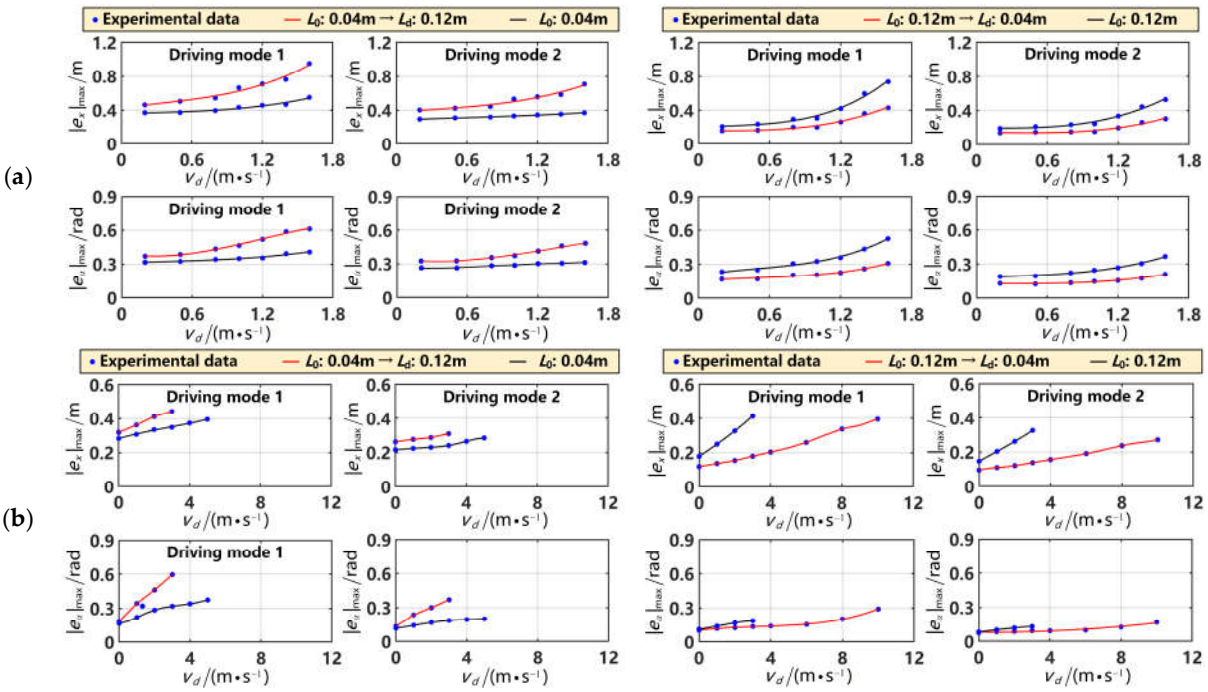

Figure 14. Experimental data of $|e_x|_{\max}$ and $|e_\alpha|_{\max}$ obtained from experiments with radial movement of the centroid. (**a**) Route 1, (**b**) Route 2.

We analyzed the experimental data of the overshoot of the control system, and the results of the analysis are presented in Table 10.

Table 10. The results of the analysis for the experimental data of the overshoot $|e|_{\max}$.

		The Pendulum Length Transitioned from L_0 to L_d	
		L_0 : 0.04m L_d : 0.12m	L_0 : 0.12m L_d : 0.04m
Route 1	κ_1	87.85% → 68.11%	135.53% → 171.28%
v_d (m/s): 0.2 → 1.6	κ_2	73.01% → 59.73%	146.72% → 187.70%
Route 2	κ_1	88.92% → 68.67%	126.32% → 182.24%
γ : 0° → 10°	κ_2	82.87% → 60.09%	137.93% → 191.13%

3.2. Energy Consumption

We evaluated the energy consumption of the spherical robot BYQ-GS under two different driving modes by means of Route 1 and Route 2. The evaluation indicators were the average output power P_i of the drive motor in each sampling period, while the BYQ-GS spherical robot moved at the expected velocity of 1 s (50 sampling periods) after motion convergence, and the method for obtaining P is shown in Equation (22). The experimental data for the evaluation indicator were obtained after motion convergence; therefore, the evaluation of energy consumption was only conducted through experiment type one.

$$P_i = \sum_{j=1}^{50} \left(\left| \tau_j n_j \right| / 9.55 \right) / 50 \tag{22}$$

where, τ_j represents the output torque of the drive motor in the jth sampling period. n_j represents the rotational speed of the drive motor in the jth sampling period [36].

In experiment type one, the trends of P are shown in Figure 15. The pendulum length, target parameters, and environmental parameters of the spherical robot were consistent under two different driving modes, $0.052\text{W} \le P_1 - P_2 \le 1.452\text{W}$ (Tables S1–S4).The

experimental data shown in Figure 15 were fitted with a mathematical model, and the fitting results can be represented by Equation (23).

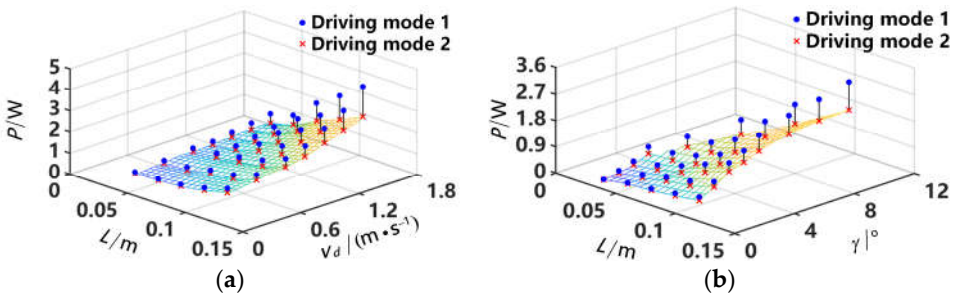

Figure 15. Experimental data of P_i obtained from experiments with different radial positions of the centroid. (**a**) Route 1, (**b**) Route 2.

$$P_i = U^{(i)}_{\text{Route}-j} = a_1x^3 + a_2y^3 + a_3x^2 + a_4y^2 + a_5x + a_6y + a_7x^2y + a_8xy^2 + a_9xy + a_{10} \quad (23)$$

The coefficients of Equation (23) are presented in Table 11. According to Equation (12), the maximum fitting accuracy of P_1 and P_2 to the experimental data is 0.024 W, which does not affect our ability to assess the trend of the experimental data.

Table 11. The coefficients for Equation (23).

		x, y	a_1	a_2	a_3	a_4	a_5	a_6	a_7	a_8	a_9	a_{10}
P_1	$U^{(1)}_{\text{Route\_1}}$	L, v_d	−1717.60	0.26	517.79	−1.36	−36.86	1.26	−10.76	16.48	−9.03	1.15
	$U^{(1)}_{\text{Route\_2}}$	L, γ	780.17	0.01	−209.84	0.05	23.04	0.20	51.62	−0.72	−3.88	−0.31
P_2	$U^{(2)}_{\text{Route\_1}}$	L, v_d	−938.25	−0.12	314.88	−0.10	−23.67	0.12	−21.45	8.44	−0.29	0.95
	$U^{(2)}_{\text{Route\_2}}$	L, γ	447.85	0.01	−122.76	0.04	15.41	0.12	41.61	−0.59	−3.10	−0.15

Based on Equation (11), we normalized the four fitted equations represented by Equation (23); that is, the energy consumption $U^{(i)}_{\text{Norm}}(L, v_d, \gamma)$ under driving modes one and two can be represented by Equation (24).

$$U^{(i)}_{\text{Norm}}(L, v_d, \gamma) = \text{Norm}\left\{\sum_{s=1}^{2} \text{Norm}\left(U^{(i)}_{x-\text{Route\_}s}\right) \Big/ 2\right\} \quad (24)$$

3.3. Locomotion Capability

As shown in Figure 6, the evaluation indicators for the locomotion capability were divided into two aspects: climbing ability and steering ability.

3.3.1. Climbing Ability

Section 3 conducts the research on motion through experiments type one and type two. For each experiment type, the experimental data were obtained through two different routes. By analyzing the experimental data obtained through Route 2, we can conclude that when the motion of the BYQ-GS spherical robot can converge, the climbing ability of the spherical robot under the inverted pendulum driving mode is equivalent to that under the lower pendulum driving mode.

Based on the data of experiment type one, the relationship between the pendulum length L and the maximum climbing angle γ is shown in Figure 16a. As the pendulum length L gradually varies from 0.04 m to 0.12 m, the maximum climbing angle γ gradually increases from 3° to 10° (Tables S3–S5). The experimental data shown in Figure 16a

were fitted with a mathematical model, and the fitting results can be represented by Equation (25). According to Equation (12), the maximum fitting accuracy of $A(L)$ to the experimental data is 0.085°, which does not affect our ability to assess the trend of the experimental data.

$$\gamma = A(L) = -10416.67L^3 + 2857.14L^2 - 152.98L + 5.20 \quad (25)$$

Based on the data of experiment type two, the relationship between the pendulum length L and the maximum climbing angle γ is shown in Figure 16b. In comparison to the motion with a constant pendulum length $L = 0.04\text{m}$, the climbing ability increases from 3° to 5° when the pendulum length L gradually increases from 0.04 m to 0.12 m at the beginning of the motion (Tables S8–S10). Similarly, in comparison to the motion with a constant pendulum length $L = 0.12\text{m}$, the climbing ability decreases from 10° to 3° when the pendulum length gradually decreases from 0.12 m to 0.04 m at the beginning of the motion.

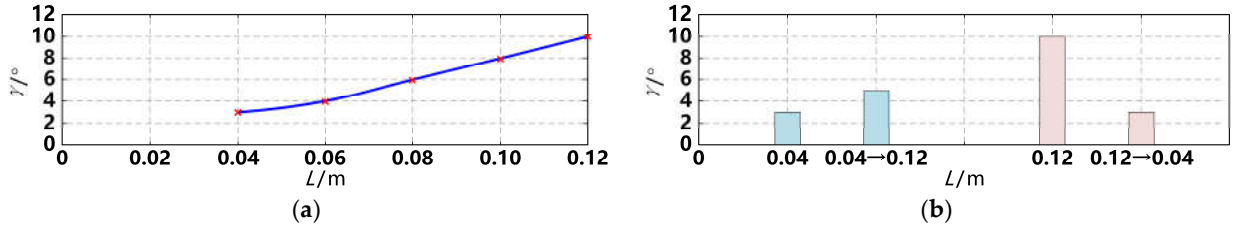

Figure 16. Experimental data of climbing ability obtained from experiments: (**a**) Different radial positions of the centroid; (**b**) Radial movement of the centroid during motion.

Based on Equation (11), we normalized the fitted equations represented by Equation (25); that is, the climbing ability $A(L)$ can be represented by Equation (26).

$$A_{\text{Norm}}(L) = \text{Norm}[1/A(L)] \quad (26)$$

3.3.2. Steering Ability

We evaluated the steering ability of the spherical robot BYQ-GS under two different driving modes by means of Route 2. Using the line connecting the target position and the initial position as a reference, the maximum distance between the motion trajectory and the line connecting the initial and target positions D_{max} is utilized to evaluate the steering capability of the spherical robot, where the distance between the real-time position (x, y) and the line connecting the initial and target positions is denoted as $D = |x - y|/\sqrt{2}$. The determination of motion convergence is based on the stability of the spherical robot within a 4 cm error range from the target position for 5 s.

Due to the necessity of obtaining experimental data, which requires the spherical robot to perform omnidirectional motion on different slope angles, we reconfigured the experimental parameters for Route 2, with the initial state of the control system set to $[x_0, y_0, \varphi_0, \theta_0, \psi_0, \alpha_0, \beta_0] = [0, 0, -\pi/2, 0, 0, 0, 0]$ and $[\dot{x}_0, \dot{y}_0, \dot{\varphi}_0, \dot{\theta}_0, \dot{\psi}_0, \dot{\alpha}_0, \dot{\beta}_0] = [0, 0, 0, 0, 0, 0, 0]$ and the desired state of the control system set to $[x_d, y_d, \alpha_d, \beta_d] = [2, 2, 0, p_\beta]$ and $[\dot{x}_d, \dot{y}_d, \dot{\alpha}_d, \dot{\beta}_d] = [0, 0, 0, 0]$.

Experiment type 1: The trends of $D_{\max}$ are shown in Figure 17. The pendulum length, target parameters, and environmental parameters of the spherical robot were consistent under two different driving modes, $0.061\text{m} \le D_{\max 1} - D_{\max 2} \le 0.219\text{m}$ (Table S5). The experimental data shown in Figure 17 were fitted with a mathematical model, and the fitting results can be represented by Equation (27).

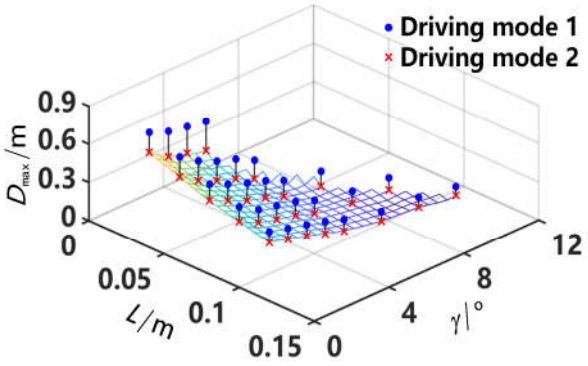

Figure 17. Experimental data of $D_{\max}$ obtained from experiments with different radial positions of the centroid.

$$D_{\max i} = B^{(i)} = a_1 x^3 + a_2 y^3 + a_3 x^2 + a_4 y^2 + a_5 x + a_6 y + a_7 x^2 y + a_8 x y^2 + a_9 x y + a_{10} \quad (27)$$

The coefficients of Equation (23) are presented in Table 12. According to Equation (12), the maximum fitting accuracy of $D_{\max 1}$ and $D_{\max 2}$ to the experimental data is 0.0082 m, which does not affect our ability to assess the trend of the experimental data.

Table 12. The coefficients for Equation (27).

		x, y	a_1	a_2	a_3	a_4	a_5	a_6	a_7	a_8	a_9	a_{10}
$D_{\max 1}$	$B^{(1)}$	L, γ	−224.59	0.01	85.44	0.01	−14.92	−0.03	1.85	−0.02	−0.05	1.37
$D_{\max 2}$	$B^{(2)}$	L, γ	−156.89	−0.01	61.45	0.01	−11.72	−0.08	0.22	−0.02	0.45	1.19

Based on Equation (11), we normalized the two fitted equations represented by Equation (27); that is, the steering ability $B^{(i)}$ under driving modes one and two can be represented by Equation (28).

$$B^{(i)}_{\text{Norm}}(L,\gamma) = \text{Norm}\left[B^{(i)}\right] \quad (28)$$

Experiment type 2: The trends of $D_{\max 1}$ and $D_{\max 2}$ are shown in Figure 18. According to the Equation (10), $\kappa_i = D_{\max i\,(L_0 \to L_d)} / D_{\max i\,(L_0)}$ (Table S10).

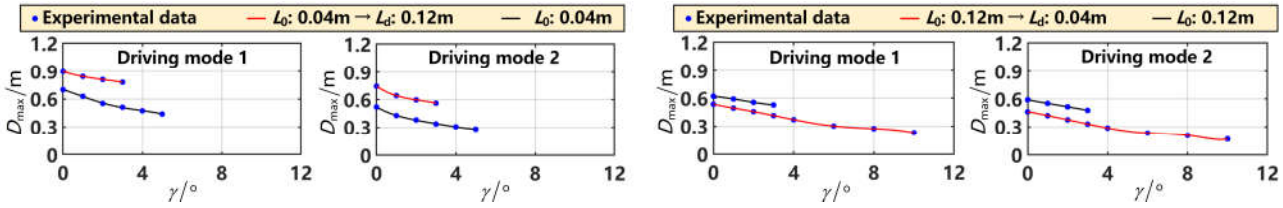

Figure 18. Experimental data of $D_{\max}$ obtained from experiments with radial movement of the centroid.

We analyzed the experimental data of the steering ability, and the results of the analysis are presented in Table 13.

Table 13. The results of the analysis for the experimental data of the convergence speed $D_{\max}$.

		The Pendulum Length Transitioned from L_0 to L_d	
		L_0 : 0.04m L_d : 0.12m	L_0 : 0.12m L_d : 0.04m
γ : 0° → 10°	κ_1	78.20% → 65.61%	116.03% → 127.29%
	κ_2	70.03% → 60.20%	127.60% → 143.91%

4. Analysis of Motion Experimental Data

We analyzed the motion control experimental data of the BYQ-GS spherical robot under two types of radial variation in the centroid, namely different radial positions of the centroid and radial movement of the centroid during motion.

4.1. Influence Law of Radial Variation in Centroid

In terms of the experimental data on control performance, locomotion capability, and energy consumption, the overall variation trend of the inverted pendulum driving mode mirrors that of the lower pendulum driving mode.

- Compared to the lower pendulum driving mode, the inverted pendulum driving mode demonstrated an advantage in response speed, overshoot, steering capability, and energy consumption while exhibiting disadvantages in convergence speed and stability. The climbing ability under two different driving modes was equivalent.
- As motion speed or task slope increased, the response speed of both driving modes remained relatively stable while the steering capability improved; however, convergence speed, stability, overshoot, and energy consumption deteriorated.
- With an increase in the distance between the centroid and the center of the sphere, the response speed, convergence speed, stability, overshoot, climbing ability, and steering capability of both driving modes improved, while energy consumption deteriorated.
- Compared to the motion where the radial position of the centroid remained constant when the radial position of the centroid gradually moved during the initial phase of motion, the response speed, convergence speed, stability, overshoot, climbing ability, steering capability, and energy consumption in either the inverted pendulum driving mode or lower pendulum driving mode varied accordingly. However, with an increased motion velocity or task slope, the degree of variation in the above indicators differed. The degree of variation in the response speed remained relatively stable, while the degree of variation in the convergence speed, stability, overshoot, climbing ability, steering capability, and energy consumption increased. Nevertheless, the degree of variation in the inverted pendulum driving mode consistently exceeded that of the lower pendulum driving mode.

4.2. Correlation Model Relating the Motion Requirements to the Radial Position of the Centroid

Based on the fitting mathematical model of the seven indicators of the BYQ-GS spherical robot, we mapped the slope angle, motion speed, and optimal pendulum length of the BYQ-GS spherical robot and the target spherical robot one by one and constructed a correlation model relating the motion requirements to the radial position of the centroid. This model ensures universality when facing spherical robots with radial variable centroid capabilities and can comprehensively consider the control performance, locomotion capability, and energy consumption according to the different requirements of the spherical robot for motion performance.

The optimal pendulum length L of the spherical robot is our ultimate target to achieve. We define the maximum climbing capability $\gamma_{\max}$ and the maximum motion speed $v_{\max}$ of the actual spherical robot in use, and the slope angle γ and the required motion speed v in specific tasks. For the BYQ-GS spherical robot, its maximum climbing capability is 10°, maximum motion speed is 4 m/s, the slope angle to be faced is $\tilde{\gamma}$, the required motion speed is $\tilde{v}$, and the range of optimal pendulum length $\tilde{L}$ is $0.04\text{m} \le \tilde{L} \le 0.12\text{m}$. We can establish the correspondence between the climbing capability $\tilde{\gamma}$ of the BYQ-GS spherical robot and the actual climbing capability γ of the spherical robot in use as $\tilde{\gamma}=10^{\circ}\gamma/\gamma_{\max}$, and the correspondence between the motion speed $\tilde{v}$ of the BYQ-GS spherical robot and the motion speed v of the actual spherical robot in use as $\tilde{v}=4v/v_{\max}$.

We define $i = 1$ as the lower pendulum driving mode and $i = 2$ as the inverted pendulum driving mode. In Equation (29), $\text{Control}^{(i)}(\tilde{L},\tilde{v},\tilde{\gamma})$ is the mathematical model of the control performance of the BYQ-GS spherical robot, which is jointly determined by the response speed fitting equation $K_{\text{Norm}}^{(i)}$ shown in Equation (14), the convergence speed fitting equation $F_{\text{Norm}}^{(i)}$ shown in Equation (17), the stability fitting equation $H_{\text{Norm}}^{(i)}$ shown in Equation (19), and the overshoot fitting equation $G_{\text{Norm}}^{(i)}$ shown in Equation (21). $\text{Move}^{(i)}(\tilde{L},\tilde{\gamma})$ is the mathematical model of the locomotion capability of the BYQ-GS spherical robot, which is jointly determined by the climbing ability fitting equation A_{Norm} shown in Equation (26), the steering capability fitting equation $B_{\text{Norm}}^{(i)}$ shown in Equation (28). $\text{Energy}^{(i)}(\tilde{L},\tilde{v},\tilde{\gamma})$ is the mathematical model of the energy consumption of the BYQ-GS spherical robot, which is determined by $U_{\text{Norm}}^{(i)}$ shown in Equation (24).

$$\text{Control}^{(i)}\left(\tilde{L},\tilde{v},\tilde{\gamma}\right)=\left(K_{\text{Norm}}^{(i)}+F_{\text{Norm}}^{(i)}+H_{\text{Norm}}^{(i)}+G_{\text{Norm}}^{(i)}\right)/4 \quad \text{Move}^{(i)}\left(\tilde{L},\tilde{\gamma}\right)=\left(A_{\text{Norm}}+B_{\text{Norm}}^{(i)}\right)/2 \quad \text{Energy}^{(i)}\left(\tilde{L},\tilde{v},\tilde{\gamma}\right)=U_{\text{Norm}}^{(i)} \tag{29}$$

We transform the problem of determining the optimal pendulum length into the optimization problem, as shown in Equation (30). According to the actual demand for motion performance during the execution of the spherical robot's task, n_1, n_2 and n_3 are respectively designated as weighting parameters, and $n_1+n_2+n_3=1$. The greater the parameter value, the more significant the corresponding requirements become. Once the value of $\tilde{\gamma}$ is given, $A^{-1}(\tilde{\gamma})$ represents the pendulum length value corresponding to $\tilde{\gamma}$ obtained based on Equation (25).

$$\begin{aligned} &\min f^{(i)}\left(\tilde{L}\right)=n_1\,\text{Control}^{(i)}\left(\tilde{L},\tilde{v},\tilde{\gamma}\right)+n_2\text{Move}^{(i)}\left(\tilde{L},\tilde{\gamma}\right)+n_3\text{Energy}^{(i)}\left(\tilde{L},\tilde{v},\tilde{\gamma}\right)\\ &\text{s.t.}\quad 0^\circ\le\tilde{\gamma}\le10^\circ \quad 0\le\tilde{v}\le4 \quad 0.04\le\tilde{L}\le0.12 \quad \tilde{L}\ge A^{-1}(\tilde{\gamma}) \end{aligned} \tag{30}$$

The optimal value of $\tilde{L}$ can be obtained by using Equation (30). By converting $\tilde{L}$ through Equation (31), the optimal pendulum length L for the actual use of the spherical robot can be obtained.

$$L=\tilde{L}\bullet L_{\max}/0.12 \tag{31}$$

where, $L_{\max}$ is the maximum pendulum length that the spherical robot can achieve.

During the task preparation phase, we first select the driving mode based on the motion performance laws of the two driving modes and the actual requirements of the task. Subsequently, considering the task requirements for motion performance, as well as the slope γ and the required motion speed v, we determine and adjust the optimal pendulum length L using Equations (30) and (31). This significantly enhances the practicality of the spherical robot when facing unstructured task environments.

5. Experimental Verification of Motion Performance Analysis Results

We have utilized the BYQ-GS spherical robot as our experimental platform and employed HSMC to accomplish motion control of the spherical robot. Taking the motion effect of keeping the pendulum length L at 0.12 m in the traditional lower pendulum driving mode as a comparison, we conducted experimental validation on the motion effect after selecting the driving mode and optimal pendulum length based on the motion performance requirements. The experimental environment was an outdoor track and field runway. We simulated two different task requirements in unstructured environments, where the slope angle γ in Equation (30) was set to 0°, and the expected velocity v_d was set to 1 m/s.

In Experiment 1, priority was given to energy consumption. Therefore, we set the weighting parameter of control performance n_1 to 0.1, the weighting parameter of locomotion capability n_2 to 0.1, and the weighting parameter of energy consumption n_3 to 0.8. In Experiment 2, priority was given to the control system's overshoot; control performance and energy consumption needed to be taken into consideration at the same time.

Therefore, we set the weighting parameter of control performance n_1 to 0.45, the weighting parameter of locomotion capability n_2 to 0.1, and the weighting parameter of energy consumption n_3 to 0.45.

According to the influence law of radial variation in the centroid in Section 4.1, the BYQ-GS spherical robot in Experiment 1 and Experiment 2 both adopted the inverted pendulum driving mode; that is, the driving mode parameter *i* in Equation (30) was set to two, and the optimization problem shown in Equation (30) was solved using the Fmincon function in MATLAB R2021a, yielding the optimal pendulum length denoted as $L=0.105\text{m}$ for Experiment 1 and $L=0.092\text{m}$ for Experiment 2 [37,38]. Throughout the experiments, the parameters of the HSMC controller were maintained consistent with Route 2, depicted in Figure 6. The pendulum length L remained constant throughout the experimental process.

The results of Experiment 1 are presented in Table 14. The objective of Experiment 1 was to optimize energy consumption; thus, a comparison was made regarding the average output power P of the drive motor in each sampling period. Based on the statistical indicators of the experimental data shown in Table 14, compared to the pendulum length $L=0.12\text{m}$ in the lower pendulum driving mode, when the spherical robot was in the lower pendulum driving mode and the pendulum length was $L=0.105\text{m}$, the decrease in P was 12.13%. Similarly, when the spherical robot was in the inverted pendulum driving mode and $L=0.105\text{m}$, the decrease in P was 33.16%. These results indicate that compared to the pendulum length $L=0.12\text{m}$ in the lower pendulum driving mode, when the spherical robot was in the inverted pendulum driving mode and the pendulum length was $L=0.105\text{m}$, the energy consumption level of the BYQ-GS spherical robot experienced a significant reduction.

Table 14. Experimental data of motion performance indicators obtained in Experiment 1.

Driving Mode	L/m	t_r /s	$\lvert e_x \rvert_{\max}$ /m	$\lvert e_\alpha \rvert_{\max}$ /rad	e_{x-rmse} /m	$e_{\alpha-rmse}$ /rad	$t_{\tau-\max}$ /s	P /W
Lower pendulum	0.12	7.83	0.202	0.206	0.909	0.167	0.54	2.078
Lower pendulum	0.105	9.03	0.334	0.283	1.124	0.178	0.66	1.826
Inverted pendulum	0.105	10.92	0.268	0.198	1.507	0.223	0.48	1.389

The objective of Experiment 2 was to optimize the control system's overshoot; control performance and energy consumption needed to be taken into consideration at the same time. Thus, a comparison was made regarding the average levels of four control performance indicators, namely the generation time of maximum torque $t_{\tau-\max}$, the motion convergence time t_r, the root mean square error of position error e_{rmse}, and the maximum absolute value of motion position error $|e|_{\max}$, while simultaneously conducting a comparison on the average output power P of the drive motor in each sampling period. Based on the statistical indicators of the experimental data shown in Table 15, compared to the pendulum length $L=0.12\text{m}$ in the lower pendulum driving mode, when the spherical robot was in the lower pendulum driving mode and the pendulum length was $L=0.092\text{m}$, the average improvement rate of the four control performance indicators was 50.92%, while the decrease in P was 23.72%. Similarly, when the spherical robot was in the inverted pendulum driving mode and $L=0.092\text{m}$, the average improvement rate of the four control performance indicators was 39.94%, while the decrease in P was 42.35%. These results indicate that compared to the pendulum length $L=0.12\text{m}$ in the lower pendulum driving mode, the spherical robot was in the inverted pendulum driving mode and the pendulum length was $L=0.092\text{m}$; although the control performance was reduced, the energy consumption performance could be improved at the same time.

Table 15. Experimental data of control performance indicators obtained in Experiment 2.

Driving Mode	L/m	t_r /s	$\|e_x\|_{\max}$ /m	$\|e_\alpha\|_{\max}$ /rad	e_{x-rmse} /m	$e_{\alpha-rmse}$ /rad	$t_{\tau-\max}$ /s	P /W
Lower pendulum	0.12	7.83	0.202	0.206	0.909	0.167	0.54	2.078
Lower pendulum	0.092	9.33	0.412	0.327	1.392	0.192	0.84	1.585
Inverted pendulum	0.092	11.28	0.302	0.213	1.692	0.246	0.59	1.198

The above two sets of experimental results demonstrate that by employing the influence law of radial variation in the centroid and the correlation model relating the motion requirements to the radial position of the centroid, it was possible to pre-select and set the driving mode and optimal pendulum length L of spherical robots. This significantly enhances the practicality of spherical robots in unstructured task environments.

6. Conclusions

Considering the influence of the inverted pendulum driving mode and the radial variation ability of the centroid on the motion of spherical robots, we utilized the traditional lower pendulum driving mode of spherical robots as a comparative reference. We conducted motion experiments with the spherical robots under different driving modes, motion velocities, and motion slope angles based on task characteristics in unstructured environments. Upon analyzing the experimental results, incorporating four control performance indicators (response speed, convergence speed, stability, and overshoot), two locomotion capability indicators (climbing ability and steering ability), and an energy consumption indicator, we analyzed the control performance, locomotion capability, and energy consumption of spherical robots under two different driving modes. The main work includes the following two aspects:

- We have summarized the influence law of radial variation in the centroid and elucidated the advantages and disadvantages of the inverted pendulum driving mode compared to the lower pendulum driving mode.
- We have developed a correlation model relating the motion requirements to the radial position of the centroid, providing a basis for the reasonable selection of the radial position of the centroid when spherical robots face different task requirements in an unstructured environment.

The above research work fills the gap in research on the impact of radial variation of the centroid on PET spherical robots' motion. This finding holds significant theoretical significance and guiding value for enhancing the diversified task execution capabilities of spherical robots in unstructured environments. When conducting the design of PET spherical robots, researchers can leverage this finding to focus on breakthroughs in the range and speed of radial variation in the centroid, as well as efficient transitions between the lower pendulum driving mode and inverted pendulum driving mode, thereby further enhancing the diversified task execution capability of spherical robots.

Supplementary Materials: The following supporting information can be downloaded at https://www.mdpi.com/article/10.3390/machines12060422/s1, Table S1: Route 1: Different expected velocity—Lower pendulum driving mode. Table S2: Route 1: Different expected velocity---Inverted pendulum driving mode. Table S3: Route 2: Different slope angles—Lower pendulum driving mode. Table S4: Route 2: Different slope angles—Inverted pendulum driving mode. Table S5: Experimental data on steering ability. Table S6: Route 1: Different expected velocity—Lower pendulum driving mode. Table S7: Route 1: Different expected velocity—Inverted pendulum driving mode. Table S8: Route 2: Different slope angles---Lower pendulum driving mode. Table S9: Route 2: Different slope angles—Inverted pendulum driving mode. Table S10: Experimental data on steering ability.

Author Contributions: Conceptualization, L.M. and H.S.; methodology, L.M.; software, M.L. and R.C.; validation, L.M. and R.C.; writing—original draft preparation, L.M.; writing—review and editing,

L.M.; visualization, M.L.; supervision, L.M. and H.S.; project administration, R.C.; funding acquisition, L.M. and H.S. All authors have read and agreed to the published version of the manuscript.

Funding: This research was funded by the National Natural Science Foundation of China (Grant No. 52205016 and 52075046).

Data Availability Statement: Data are contained within the article and Supplementary Materials.

Acknowledgments: The authors acknowledge the support from the Hanxu Sun, Minggang Li, and Rui Chang for their assistance in the research.

Conflicts of Interest: The authors declare that they have no known competing financial interest or personal relationship that could have appeared to influence the work reported in this manuscript.

References

1. Mahboubi, S.; Fakhrabadi, M.M.S.; Ghanbari, A. Design and Implementation of a Novel Hybrid Quadruped Spherical Mobile Robot. *Robot. Auton. Syst.* **2013**, *61*, 184–194.
2. Chang, W.J.; Chang, C.L.; Ho, J.H.; Lin, P.C. Design and Implementation of a Novel Spherical Robot with Rolling and Leaping Capability. *Mech. Mach. Theory* **2022**, *171*, 104747.
3. Asama, J.; Burkhardt, M.R.; Davoodi, F.; Burdick, J.W. Design investigation of a coreless tubular linear generator for a Moball: A spherical exploration robot with wind-energy harvesting capability. In Proceedings of the 2015 IEEE International Conference on Robotics and Automation (ICRA), Seattle, WA, USA, 26–30 May 2015; pp. 244–251.
4. Artusi, M.; Potz, M.; Aristizabal, J.; Menon, C.; Cocuzza, S.; Debei, S. Electroactive Elastomeric Actuators for the Implementation of a Deformable Spherical Rover. *IEEE/ASME Trans. Mechatron.* **2011**, *16*, 50–57.
5. Kamon, S.; Bunathuek, N.; Laksanacharoen, P. A Three-Legged Reconfigurable Spherical Robot No.3. In Proceedings of the 30th IEEE International Conference on Robot & Human Interactive Communication (RO-MAN), Vancouver, BC, Canada, 23 August 2021; pp. 426–433.
6. Bicchi, A.; Balluchi, A.; Prattichizzo, D.; Gorelli, A. Introducing the "SPHERICLE": An Experimental Testbed for Research and Teaching in Nonholonomy. In Proceedings of the 2002 IEEE International Conference on Robotics and Automation(ICRA), Albuquerque, NM, USA, 6 August 2002; pp. 2620–2625.
7. Zhou, T.; Xu, Y.G.; Wu, B. Smooth Fractional Order Sliding Mode Controller for Spherical Robots with Input Saturation. *Appl. Sci.* **2020**, *10*, 2117.
8. Chen, W.H.; Chen, C.P.; Tsai, J.S. Design and Implementation of a Ball-Driven Omnidirectional Spherical Robot. *Mech. Mach. Theory* **2013**, *68*, 35–48.
9. Ghariblu, H. A New Mobile Ball Robot-Dynamic Modeling and Simulation. *Appl. Math. Model.* **2015**, *39*, 3103–3115.
10. Zhan, Q.; Li, W. Research Progress and Development Trend of Spherical Mobile Robots. *Chin. J. Mech. Eng.-CN* **2019**, *55*, 1–17.
11. Sanchez, S.S.D.; Gomez, G.R.; Carranza, J.M. Control of a Spherical Robot Rolling over Irregular Surfaces. *J. Univers. Comput. Sci.* **2023**, *29*, 1198–1216.
12. Yoon, J.C.; Ahn, S.S.; Lee, Y.J. Spherical Robot with New Type of Two-Pendulum Driving Mechanism. In Proceedings of the 2011 IEEE 15th International Conference on Intelligent Engineering Systems (INES), Poprad, Slovakia, 14 July 2011; pp. 275–279.
13. Mahboubi, S.; Fakhrabadi, M.S.; Ghanbari, A. Design and Implementation of a Novel Spherical Mobile Robot. *J. Intell. Robot. Syst.* **2013**, *71*, 43–64.
14. DeJong, B.P.; Karadogan, E.; Yelamarthi, K.; Hasbany, J. Design and Analysis of a Four-Pendulum Omnidirectional Spherical Robot. *J. Intell. Robot. Syst.* **2017**, *86*, 3–15.
15. Yue, M.; Liu, B.Y. Disturbance Adaptive Control for an Underactuated Spherical Robot Based on Hierarchical Sliding-Mode Technology. In Proceedings of the 2012 IEEE 3th Chinese Control Conference, Hefei, China, 24 December 2012; pp. 4787–4791.
16. Cai, Y.; Zhan, Q.; Xi, X. Path Tracking Control of a Spherical Mobile Robot. *Mech. Mach. Theory* **2012**, *51*, 58–73.
17. Cai, Y.; Zhan, Q.; Yan, C.X. Two-State Trajectory Tracking Control of a Spherical Robot Using Neurodynamics. *Robotica* **2012**, *30*, 195–203.
18. Cai, Y.; Zhan, Q.; Xi, X. Neural Network Control for the Linear Motion of a Spherical Mobile Robot. *Int. J. Adv. Robot. Syst.* **2011**, *8*, 79–87.
19. Ma, L.; Sun, H.X.; Song, J.Z. Fractional-Order Adaptive Integral Hierarchical Sliding Mode Control Method for High-Speed Linear Motion of Spherical Robot. *IEEE Access* **2020**, *9*, 66243–66256.
20. Addanki, S.; Prapanch, S.; Sairam, V.; Kumar, V. AURDION—The Spherical Robot. In Proceedings of the 2016 IEEE 2nd International Conference on Technological Innovations in Ict for Agriculture & Rural Development (TIAR), Chennai, India, 15–16 July 2016; pp. 151–157.
21. Ma, L.; Sun, H.X.; Li, M.G.; Sun, P.; Zhang, W.Z.; Long, B.Z.; Shi, H.W. Design and Motion Analysis of a Spherical Robot Having the Ability to Change the Centroid Radially. *Chin. J. Mech. Eng.-CN* **2022**, *58*, 44–56.
22. Ali, H.M.Y.; Sheikh, M.N.; Hadi, M.N.S. Near-Surface Mounting-Strengthened Reinforced Concrete Beams Incorporating Glass Fiber-Reinforced Polymer Channels. *ACI Struct. J.* **2023**, *120*, 75–86.

23. Ma, L.; Sun, H.X.; Lan, X.J. Dynamic Response and Damage Assessment of Spherical Robot GFRP Spherical Shell under Low Velocity Impact. *Mater. Test.* **2020**, *62*, 703–715.
24. Talaeizadeh, M.; Forootan, M.; Zabihi, M.; Pishkenari, H.N. Comparison of Kane's and Lagrange's Methods in Analysis of Constrained Dynamical Systems. *Robotica* **2020**, *38*, 2138–2150.
25. Ba, P.D.; Hoang, Q.D.; Lee, S.G.; Nguyen, T.H.; Duong, X.Q.; Tham, B.C. Kinematic Modeling of Spherical Rolling Robots with a Three-Omnidirectional-Wheel Drive Mechanism, In Proceedings of the 2020 IEEE 20th International Conference on Control (ICCAS), Busan, Republic of Korea, 13–16 October 2020; pp. 463–466.
26. Zeinali, M.; Notash, L. Adaptive Sliding Mode Control with Uncertainty Estimator for Robot Manipulators. *Mech. Mach. Theory* **2010**, *45*, 80–90.
27. Efe, M.O. Integral Sliding Mode Control of a Quadrotor with Fractional Order Reaching Dynamics. *Trans. Inst. Meas. Control* **2011**, *33*, 985–1003.
28. Ladaci, S.; Charef, A. On Fractional Adaptive Control. *Nonlinear Dynam*. **2006**, *43*, 365–378.
29. Yu, T.; Sun, H.X.; Jia, Q.X.; Zhang, Y.H.; Zhao, W. Dynamics and Trajectory Tracking of a Spherical Rolling Robot on an Inclined Plane. In Proceedings of the 2013 International Conference on Mechanics, Dynamic Systems and Materials Engineering (MDSME), Guangzhou, China, 24–25 November 2012; pp. 151–154.
30. Yue, M.; Liu, B.Y.; An, C.; An, C.; Sun, X.J. Extended State Observer-Based Adaptive Hierarchical Sliding Mode Control for Longitudinal Movement of a Spherical Robot. *Nonlinear Dynam*. **2014**, *78*, 1233–1244.
31. Yang, X.T.; Zou, A.K.; Cao, J.D.; Lai, Y.Z.; Zhang, J.L. Systemic Risk Prediction Based on Savitzky-Golay Smoothing and Temporal Convolutional Networks. *Electron. Res. Arch*. **2023**, *31*, 2667–2688.
32. Schettino, B.M.; Duque, C.A.; Silveira, P.M. Current-Transformer Saturation Detection Using Savitzky-Golay Filter. *IEEE Trans. Power Deliv.* **2016**, *31*, 1400–1401.
33. Shott, S. Nonparametric Statistics. *JAVMA-J. Am. Vet. Med. Assoc.* **1991**, *198*, 1126–1128.
34. Michael, S. Parameterization and Smooth Approximation of Surface Triangulations. *Comput. Aided Geom. Des.* **1997**, *14*, 231–250.
35. Yalamov, P.Y.; Yuan, J.Y. A Successive Least Squares Method for Structured Total Least Squares. *J. Comput. Math.* **2003**, *21*, 463–472.
36. Öztürk, B.; Ugur, L.; Yildiz, A. Investigation of Effect on Energy Consumption of Surface Roughness in X-Axis and Spindle Servo Motors in Slot Milling Operation. *Measurement* **2019**, *139*, 92–102.
37. Ji, W.; Shao, T.Y. Finite Element Model Updating for Improved Box Girder Bridges with Corrugated Steel Webs Using the Response Surface Method and Fmincon Algorithm. *KSCE J. Civ. Eng*. **2021**, *25*, 586–602.
38. Albaghdadi, A.M.; Baharom, M.B.; Sulaiman. A.B. Parameter Design Optimization of the Crank-Rocker Engine Using the FMINCON Function in MATLAB. *Mater. Sci. Eng. R* **2021**, *1088*, 012072.

Disclaimer/Publisher's Note: The statements, opinions and data contained in all publications are solely those of the individual author(s) and contributor(s) and not of MDPI and/or the editor(s). MDPI and/or the editor(s) disclaim responsibility for any injury to people or property resulting from any ideas, methods, instructions or products referred to in the content.